



國立臺灣大學工學院材料科學與工程學系暨研究所

碩士論文

Department of Material Science and Engineering

College of Engineering

National Taiwan University

Master's Thesis

磁性穿隧元件之薄膜調整與電性研究

Modulation of Thin Film and Research of Electrical Property for
Magnetic Tunnel Junction

黃文翰

Wen-Han Huang

指導教授：白奇峰 博士

Advisor: Chi-Feng Pai, Ph.D.

中華民國 113 年 7 月

July, 2024

國立臺灣大學碩士學位論文
口試委員會審定書

MASTER'S THESIS ACCEPTANCE CERTIFICATE
NATIONAL TAIWAN UNIVERSITY

(論文中文題目) 磁性穿隧元件之薄膜調整與電性研究
(Chinese title of Master's Thesis)

(論文英文題目) Modulation of Thin Film and Research of
(English title of Master's Thesis) Electrical Property for Magnetic Tunnel Junction

本論文係 **黃文翰** (R10527A25) 在國立臺灣大學材料科學與工程學系國際應用材料工程碩士班完成之碩士學位論文，於民國 113 年 7 月 29 日 承下列考試委員審查通過及口試及格，特此證明。

The undersigned, appointed by the Department / Graduate Institute of Materials Science and Engineering International Institute of Applied Materials Engineering on 29th/July/2024 have examined a Master's Thesis entitled above presented by **Huang, Wen-Han** (R10527A25) candidate and hereby certify that it is worthy of acceptance.

口試委員
Oral examination committee: 白奇峰 白奇峰
(指導教授 Advisor)

魏拯華 魏拯華

薛文証 薛文証

系(所、學位學程) 主管 Director: 蔡豐羽 蔡豐羽

誌謝



碩士兩年的時光匆匆飛逝，我很幸運能加入白奇峰教授的 SCREAM 團隊，深入研究自旋電子學和磁性記憶體領域。首先，我要由衷感謝白老師。除了教導我們有關自旋電子學的知識外，還提供了許多研究建議、指導和經驗分享。白老師耐心的指導讓我受益匪淺，同時也給予我們學生極大的工作彈性，讓我們能自由調整步調。

接下來，我要特別感謝唯邦學長、宇豪學長和東岳學長，他們在兩年間一直陪伴著我，提供我各種幫助，包括實驗儀器測量、製程設備的學習訓練，以及數據處理和作圖技巧等。同樣地，感謝實驗室的同屆同學，瑞旭、孟頡、沛汝、聖文、哲睿，不僅在研究方面提供了許多儀器測量上的幫助，交換實驗資訊，也是課堂學習的好隊友。當然，還有平常一起在實驗室聊天的學弟妹詠絢、翊文、書鋒、智晨、冠宇，讓實驗室多了更多活潑的氣氛。

最後，我要感謝我的家人。不僅在經濟方面給予我支持，還教導了我面對失敗和挫折時應有的態度，在實驗不斷失敗的時候不斷鼓勵和支持我。這兩年的經驗讓我深刻體會到，無論是研究、論文，還是未來的挑戰，僅靠自己是無法突破的。除了自身的努力，身邊的親朋好友的幫助也是不可或缺的要素。

中文摘要



磁阻式隨機存取記憶體是未來潛在的一種記憶體技術，其優勢在於非揮發性。磁穿隧結是磁阻式隨機存取記憶體的基本單元。在磁穿隧結的所有機制中，自旋軌道耦合型-磁穿隧結和磁穿隧阻比型-磁穿隧結是製造最有效率磁穿隧結的兩個關鍵元素。自旋軌道耦合型-磁穿隧結提供了一種低能耗的寫入方式，使用鎢作為自旋電子來源層。另一方面，磁穿隧阻比型-磁穿隧結理論發現鈷鐵硼/氧化鎂/鈷鐵硼系列能夠提供最高的磁阻比，使得不同狀態可以輕易被區分。基於這兩個關鍵元素，我們堆疊了 鈦/鎢/鈷鐵硼/氧化鎂/鈷鐵硼/鎢/鈦 的薄膜結構，並調整到最佳參數。為了在低功耗和高耐久性之間取得平衡，合理的矯頑場對於磁穿隧結的兩個磁性層（自由層和固定層）至關重要。在這篇論文中，我們展示了擁有垂直異向性和水平異向性的磁穿隧結膜厚調整，以及基於這些調整的矯頑場變化。此外，我們還展示了磁穿隧結的製造過程。未來，這些裝置不僅可以作為記憶體使用，還有可能用於模擬人工智能領域中生物神經元和突觸的行為。

關鍵字：磁阻式隨機存取記憶體、磁穿隧結、自旋軌道耦合、磁阻比、鈷鐵硼/氧化鎂/鈷鐵硼系列。

ABSTRACT



Magnetoresistive Random Access Memory (MRAM) is a potential memory in the future, with its advantage on non-volatility. Magnetic tunnel junctions (MTJs) are the basic unit in MRAM. Among all mechanisms of MTJs, spin-orbit-torque MTJ (SOT-MTJ) and tunneling magnetoresistance (TMR) - based MTJ are two key elements in producing effective MTJs. SOT-MTJ provides a low-energy-consuming way to write in MTJs, using tungsten as its spin source layer. On the other hand, TMR-based MTJ suggests that CoFeB/MgO/CoFeB series provide the highest TMR ratio, where different states can easily be distinguished. Based on the two key elements, we deposit a stack of Ta/W/CoFeB/MgO/CoFeB/W/Ta thin film and modulate it to the best parameters. In order to strike the balance between low power consumption and high endurance, it is crucial to acquire a reasonable coercivity field (H_c) for the two magnetic layers, free layer and fix layer, in MTJs. In this thesis, we demonstrated the thickness modulations of PMA and IMA MTJs, and the H_c change based on these modulations. Also, we demonstrated the process of MTJ fabrication. In the future, these devices can not only be memories, but potentially also be used in simulating behaviors of biological neurons and synapses in artificial intelligence field.

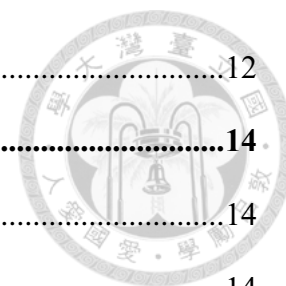
Keywords: Magnetoresistive Random Access Memory (MRAM), Magnetic tunnel junction (MTJ) MTJ, Spin-orbit-torque (SOT), Tunneling magnetoresistance (TMR), CoFeB/MgO/CoFeB series

CONTENTS

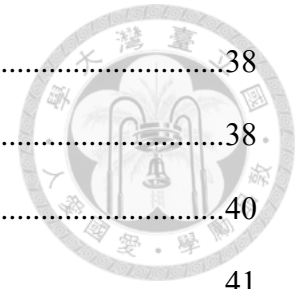


口試委員會審定書	#
誌謝	i
中文摘要	ii
ABSTRACT	iii
CONTENTS	iv
LIST OF FIGURES	vii
LIST OF TABLES	xii
Chapter 1 Introduction.....	1
1.1 Magnetization	1
1.1.1 Ferromagnetic (FM) Materials	1
1.1.2 In-plane Magnetic Anisotropy (IMA) and Perpendicular Magnetic Anisotropy (PMA)	2
1.2 Magnetoresistance (MR)	4
1.2.1 Giant Magnetoresistance (GMR)	4
1.2.2 Tunneling Magnetoresistance (TMR)	5
1.3 Hall Effect.....	7
1.3.1 Anomalous Hall Effect (AHE).....	7
1.3.2 Spin Hall Effect (SHE).....	8
1.4 Magnetic Tunnel Junctions (MTJ).....	8
1.4.1 Spin-Transfer Torque (STT) MTJ	8
1.4.2 Spin-Orbit Torque (SOT) MTJ.....	10
1.4.3 Resistance Area (RA) product.....	11

1.5	Motivation.....	12
Chapter 2	Sample Preparation	14
2.1	Thin Film Deposition.....	14
2.1.1	Magnetron Sputtering and Annealing	14
2.2	Post Process for Device Manufacture.....	15
2.2.1	Photolithography	15
2.2.2	Ion Beam Etching (IBE).....	15
2.2.3	Electron Beam Evaporator (EBE).....	17
2.3	Device Fabrication.....	17
2.3.1	MTJ Fabrication	17
Chapter 3	Measurement	22
3.1	Thin Film Measurement	22
3.1.1	Magneto-Optical Effect (MOKE)	22
3.2	Secondary Ion Mass Spectrometry (SIMS)	23
3.3	MTJ Measurement.....	25
3.3.1	TMR Measurement	25
Chapter 4	Results and Discussion.....	26
4.1	PMA Thin Film.....	26
4.1.1	Half MTJ Structure	26
4.1.2	Full MTJ Structure	27
4.1.3	Short Conclusion.....	29
4.2	IMA Thin Film Annealed without External Field.....	30
4.2.1	Half MTJ Structure	30
4.2.2	Full MTJ Structure	33
4.2.3	Short Conclusion.....	38



4.3	IMA Thin Film Annealed with External Field.....	38
4.3.1	Half MTJ Structure	38
4.3.2	Full MTJ Structure	40
4.3.3	Short Conclusion.....	41
4.4	Failure Analysis for MTJ Devices	42
4.4.1	Case 1 of Stop-on-W	42
4.4.2	Case 2 of Stop-on-W	51
4.4.3	Case 3 Stop-on-MgO.....	53
4.4.4	Short Conclusion.....	58
Chapter 5	Summary.....	60
	REFERENCE	62



LIST OF FIGURES



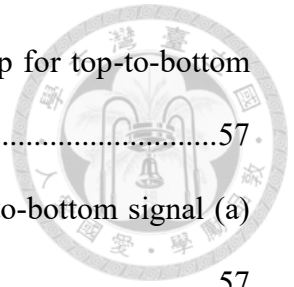
Figure 1.1 Schematic representation of ferromagnetic (FM) material.[1]	2
Figure 1.2 Illustration of hysteresis loop and coercivity field (H_c) [2]	2
Figure 1.3 The PMA property of CoFeB/MgO depends on its thickness.[6]	3
Figure 1.4 Illustration of a GMR signal[7].....	4
Figure 1.5 Schematic of Mott's model (a) In P state, spin-up electrons passes through the two FM layers without scattering (b) In AP state, both spin-up and spin-down electrons are mostly scattered. [8, 9]	5
Figure 1.6 Illustration of a TMR signal[20]	6
Figure 1.7 A schematic of (a) incoherent tunneling in amorphous Al-O barrier and (b) coherent tunneling dominated by Δ_1 in Fe/MgO/Fe structure[18]	6
Figure 1.8 The Hall effect family[23].....	7
Figure 1.9 With spin Hall effect, incoming charge current can be converted into spin current.[28]	8
Figure 1.10 Schematic of an STT MTJ[32].....	9
Figure 1.11 Illustration of a double loop signal and a minor loop[33].....	10
Figure 1.12 Schematic of an SOT MTJ with W, as its spin source layer[37].....	11
Figure 1.13 RA product shows an exponential trend to MgO thickness.[20]	12
Figure 2.1 Illustration of magnetron sputtering[46]	14
Figure 2.2 Common process of photolithography[47]	15
Figure 2.3 Schematic of ion beam etching[48]	16
Figure 2.4 Illustration of E-beam evaporator[49].....	17
Figure 2.5 Mask patterns of different MTJ fabrication steps (a) 1 st lithography (b) 2 nd	

lithography (c) 3 rd lithography.....	18
Figure 2.6 Schematic of different MTJ fabrication steps (a) 1 st lithography (b) 1 st etching (c) thin film after 1 st process (d) 2 nd lithography (e) 2 nd etching (f) E-gun evaporation (g) thin film after 2 nd process (h) 3 rd lithography and electrode.....	20
Figure 2.7 (a) The definition of pillar size (b) The arrangement of 30 devices	21
Figure 3.1 Three geometries of MOKE includes (a) Polar (b) Longitudinal and (c) Transverse.[50]	23
Figure 3.2 Schematic of MOKE setup[51].....	23
Figure 3.3 Schematic of SIMS detection during IBE[52]	24
Figure 3.4 SIMS provides real-time signal during etching[52].....	25
Figure 3.5 Schematic of current flow during TMR measurement.....	25
Figure 4.1 (a) Among all thicknesses with good hysteresis loop, CFB(1.6) shows the smallest H_c . (b) For $1.6 \leq t_{CFB} \leq 2.0$ nm, it shows the largest H_c	27
Figure 4.2 It doesn't show double loop after combining two half layers into a full MTJ structure, with fix layer CFB thickness from 1.6 to 2.0.	28
Figure 4.3 Since it doesn't show double loop after modulating CFB thickness, we therefore modulate MgO thickness.....	29
Figure 4.4 It shows double loop after modulating W thickness.	29
Figure 4.5 (a) CFB(3) shows the smallest H_c . (b) H_c are large enough for CFB thicker than 4nm.	31
Figure 4.6 (a)(b) As-deposited thin films show smaller H_c . These thin films are the same structures as in Figure 4.5.....	32
Figure 4.7 H_c extracted from Figure 4.5 and Figure 4.6. (a)(b) After annealing, coercivity significantly increases.....	32

Figure 4.8 H_c extracted from Figure 4.7. (a) For CFB(3), no angle dependence is observed. (b)(c) For CFB(4) and (4.5), although H_c fluctuates at different angle, there are no evident regulation.	33
Figure 4.9 It doesn't show double loop for free-CFB(3) and free-CFB(3.5).....	34
Figure 4.10 (a) After annealing, it shows double loops for $1.2 \leq t_{MgO} \leq 1.5$ nm for fix-CFB(4). (b) It does not show evident double loop for fix-CFB(5).....	34
Figure 4.11 For thinner MgO thickness t_{MgO} (1), it shows double loops for fix-CFB thickness from 4–4.8 nm.....	35
Figure 4.12 Samples are annealed for (a) 20 (b) 30 (c) 40 (d) 50 minutes. With longer annealing time, the double loops become sharper.	36
Figure 4.13 (a)(b)(c)(d) Minor loop of the same thin films in Figure 4.12.	37
Figure 4.14 (a) For bottom half MTJ, easy and hard axis can be easily distinguished, but coercivity of easy axis does not increase after annealing with external field. (b) For top half MTJ, hysteresis loops don't show evident easy and hard axes behaviors after annealing.....	39
Figure 4.15 (a) For the extracted H_c of bottom half structure, the regulation of easy and hard axes are clearly shown. (b) For the top half of MTJ, the coercivity does not have strong regulation to angle.....	39
Figure 4.16 (a)(b) It shows double loops only for MgO thickness at 0.9nm, after annealing for 40 minutes.	40
Figure 4.17 (a)(b)(c)(d) H_c shows similar results for different annealing time.	41
Figure 4.18 MOKE signal of four samples. (a)(b) PMA sample with one single hysteresis loop. (c)(d) PMA sample with double hysteresis loops.....	43
Figure 4.19 OM images of 1 st lithography (a) Sample 1 (b) Sample 2 (c)(d) Sample 3 (e)(f) Sample 4	44

Figure 4.20 SIMS signal of 1 st Etching (a) Sample 1 and 2 (b) Sample 3 and 4.....	45
Figure 4.21 OM images of 2 nd lithography (a) Sample 1 (b) Sample 2 (c) Sample 3 (d) Sample 4	46
Figure 4.22 2 nd etching (a)(b)(c)(d) stands for sample 1 to 4 respectively.....	46
Figure 4.23 OM image of 3 rd lithography (a) Sample 3 (b) Sample 4	47
Figure 4.24 Top-to-bottom signal for sample 2 (a) 12x10 μm^2 (b) 12x6 μm^2	48
Figure 4.25 Bottom-to-bottom signal for sample 2 (a) 12x10 μm^2 (b) 12x6 μm^2	48
Figure 4.26 Top-to-bottom signal for sample 3 (a) 12x10 μm^2 (b) 12x6 μm^2 (c) 10x8 μm^2 (b) 8x6 μm^2	49
Figure 4.27 Bottom-to-bottom signal for sample 3 (a) 12x10 μm^2 (b) 10x8 μm^2 (c) 8x6 μm^2	50
Figure 4.28 Top-to-bottom signal for sample 3 (a) Resistance relation to pillar area (b) TMR ratio	50
Figure 4.29 Bottom-to-bottom signal for sample 3 (a) Resistance relation to pillar area (b) TMR ratio	51
Figure 4.30 1 st etching signal of the sample	51
Figure 4.31 2 nd etching signal of the sample	52
Figure 4.32 Top-to-bottom signal (a) 12x10 μm^2 (b) 10x8 μm^2 (c) 4x8 μm^2 (d) 2x6 μm^2	53
Figure 4.33 Bottom-to-bottom signal (a) 12x10 μm^2 (b) 10x8 μm^2 (c) 4x8 μm^2	53
Figure 4.34 1 st etching signal of case stop-on-MgO.....	54
Figure 4.35 (a)(b)(c)(d) OM images of 2 nd lithography	55
Figure 4.36 2 nd etching signal of case stop-on-MgO.....	55
Figure 4.37 OM images of 2 nd E-gun evaporation	56
Figure 4.38 OM images of 3 rd lithography.....	56

Figure 4.39 (a)(b) One device of sample MgO 1.0 shows TMR loop for top-to-bottom detection.....	57
Figure 4.40 Fail devices of sample MgO 0.9 and MgO 1.0 for top-to-bottom signal (a) MgO0.9 12x10 μm^2 (b) MgO1.0 10x10 μm^2	57
Figure 4.41 Fail devices of sample MgO 1.0 for bottom-to-bottom signal, 12x8 μm^2 ...	58
Figure 4.42 Resistance distribution of sample MgO 0.9 and MgO 1.0.....	58



LIST OF TABLES



Table 2.1 The devices are arranged based on their pillar sizes as Figure 2.7.....21

Chapter 1 Introduction



1.1 Magnetization

1.1.1 Ferromagnetic (FM) Materials

Considering the magnetic properties, materials can be categorized into ferromagnetic (FM), ferrimagnetic, paramagnetic and diamagnetic materials. In our experiments, we mainly focus on the properties of ferromagnetic materials, e.g. CoFeB (CFB). For ferromagnetic materials, all segments are aligned to the same direction as shown in Figure 1.1.

In Figure 1.2, we can attain hysteresis loop by scanning external field over a FM material. The coercivity field (H_c) is the applied external field when magnetization (M) is zero, which depicts how hard switching magnetization is. It is worth noticing that when the external field is applied to the same direction of magnetization, it is called easy axis; that is, when we scan z field for thin films with perpendicular magnetic anisotropy (PMA), and x or y field for thin films with in-plane magnetic anisotropy (IMA), it is called easy axis. IMA and PMA will be further discussed in the next section Chapter 1.1.2.

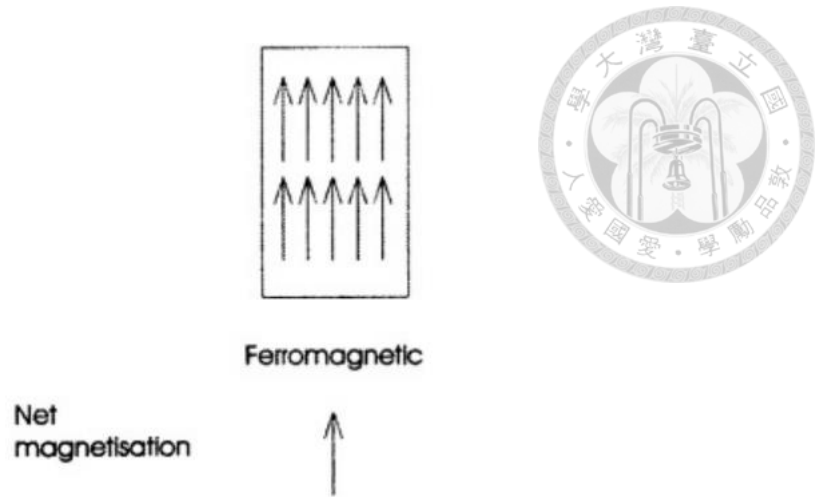


Figure 1.1 Schematic representation of ferromagnetic (FM) material.[1]

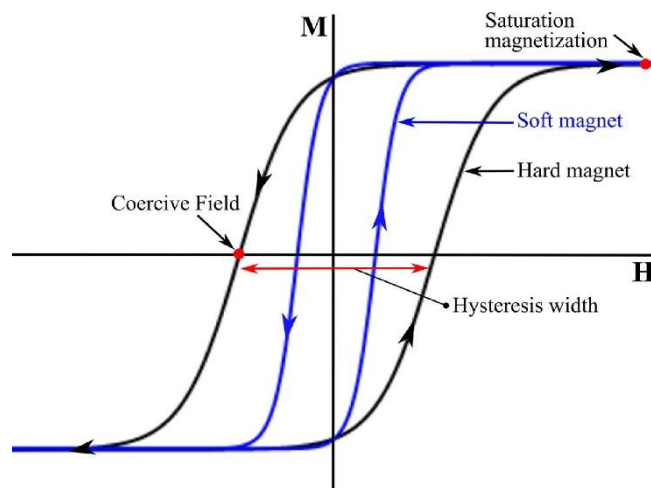
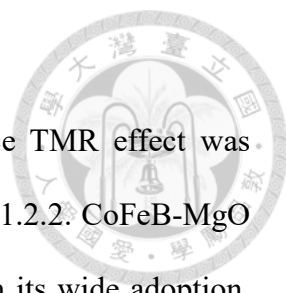


Figure 1.2 Illustration of hysteresis loop and coercivity field (H_c) [2]

1.1.2 In-plane Magnetic Anisotropy (IMA) and Perpendicular Magnetic Anisotropy (PMA)

IMA and PMA property refer to the direction of magnetic anisotropy of a thin film. In our experiment, the magnetic anisotropy depends on the thickness of the CoFeB (CFB) layer. When the CoFeB layer is thin enough, 1.6nm to 2.0nm, approximately, PMA dominates the anisotropy. On the contrary, IMA property dominates when CoFeB layer is



thicker than 3nm.

IMA systems have a longer history than PMA systems, since TMR effect was proposed in 1975[3]. TMR effect will be discussed later in Chapter 1.2.2. CoFeB-MgO system is so far the most common system for MTJ structures. With its wide adoption, this system has a highest TMR ratio of 604% recorded in 2008[4]. As for the PMA system, the first system of Co/Pd is proposed in 1985[5]. Later, the first PMA system of CoFeB/MgO was proposed, in a Ta/CoFeB/MgO/CoFeB/Ta structure with a high TMR ratio of 120% in 2010[6].

This direction of anisotropy results from the competition between interfacial perpendicular anisotropy of CoFeB/MgO surface and the in-plane bulk anisotropy. Since the interfacial anisotropy is inversely proportional to its effective anisotropy, perpendicular anisotropy only exists when the layer is thin enough. The anisotropy is demonstrated as Figure 1.3, when CoFeB has an easy axis on in-plane direction at 2.0 nm, and an easy axis on out-of-plane direction at 1.3 nm.

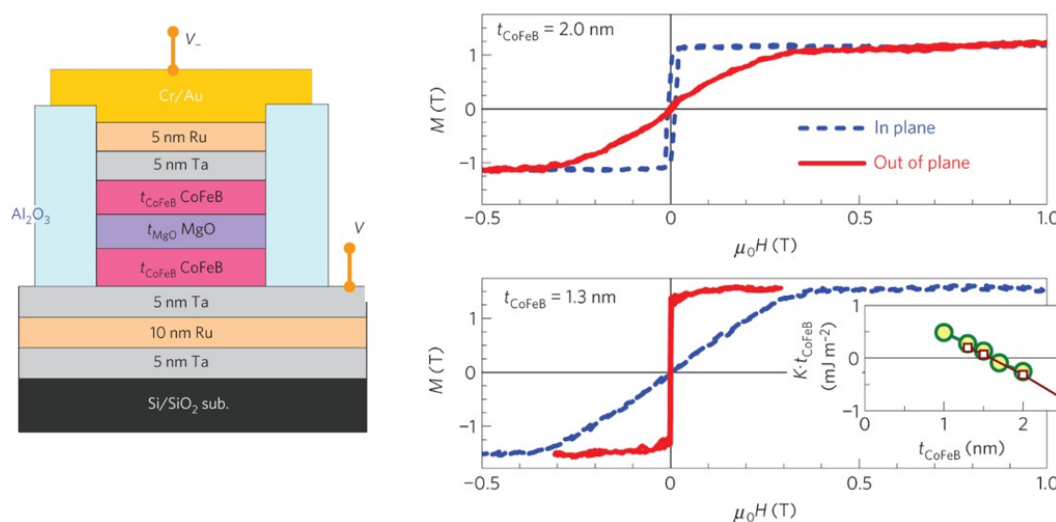


Figure 1.3 The PMA property of CoFeB/MgO depends on its thickness.[6]



1.2 Magnetoresistance (MR)

1.2.1 Giant Magnetoresistance (GMR)

Giant magnetoresistance is one crucial origin of magnetoresistance. Proposed in 1988[7], GMR usually consists of three layers, FM/normal metal (NM)/FM. When the two FM layers are in parallel (P) or antiparallel (AP) state, they show different resistance, which is referred to as “GMR ratio”. Due to Mott’s explanation in Figure 1.5, spin-up electrons pass through the two FM layers without scattering in P state, while all electrons are scattered in AP state[8, 9]. GMR ratio is usually less than 70% in room temperature, including Co/Cu - 65%[10], Ni₈₀Fe₂₀/Cu - 18%[11], Ni₈₀Fe₂₀/Ag - 17%[12] and Ni₈₀Fe₂₀/Au - 12%[13], the highest recorded in each structure.

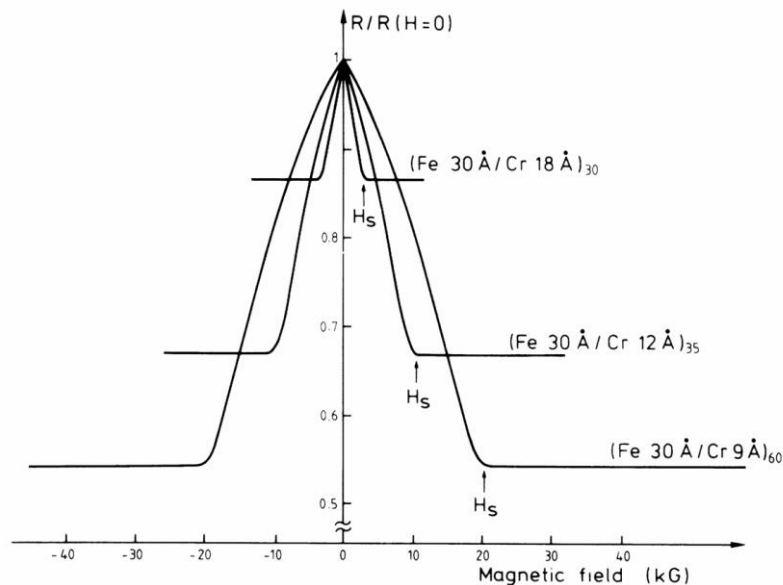


Figure 1.4 Illustration of a GMR signal[7]

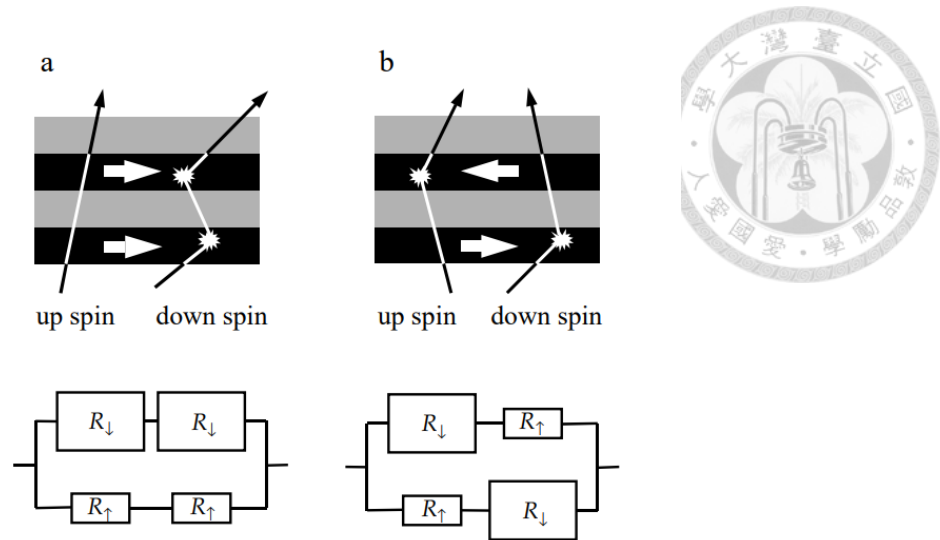


Figure 1.5 Schematic of Mott's model (a) In P state, spin-up electrons passes through the two FM layers without scattering (b) In AP state, both spin-up and spin-down electrons are mostly scattered. [8, 9]

1.2.2 Tunneling Magnetoresistance (TMR)

Similar to GMR, TMR also consists of three layers. TMR effect was proposed by M. Julliere in 1975[3]. Instead of the sandwich FM/NM/FM structure in GMR, the three layers in TMR are FM/insulator/FM. TMR ratio is usually much larger than GMR ratio, and was recorded 604% for in-plane systems, and 120% for out-of-plane systems[4, 6], as mentioned in Chapter 1.1.2. Both records are found in CoFeB/MgO/CoFeB series, making CoFeB/MgO system a common TMR structure. Since TMR plays a crucial role in MTJs, there are many reviews about the effect[14, 15].

TMR ratio is defined as the ratio difference between P and AP state, and can be explained by spin-dependent tunneling and Julliere model[3, 16]. When the sandwich structure is at P state, the electrons with same spin are easier to tunnel, e.g., spin-up and spin-up state of the two FM layer, and results in a lower resistance. On the contrary, when the sandwich structure is at AP state, only a part of electrons can act as carriers, and results

in a high resistance, as shown in Figure 1.6. A giant TMR ratio can be achieved when the lattice structure of the three layers matches, and perform coherent tunneling, as shown in Figure 1.7(b)[17, 18]. By *ab initio* calculation, it is theoretically predicted that Fe/MgO/Fe sandwich structure could achieved a TMR ratio exceeding 1000%. Experimentally, CoFeB/MgO/CoFeB shows the highest TMR ratio after ex-situ annealing, when the three layer are all bcc (001)-oriented, and Δ_1 symmetry Bloch state dominates coherent tunneling[19].

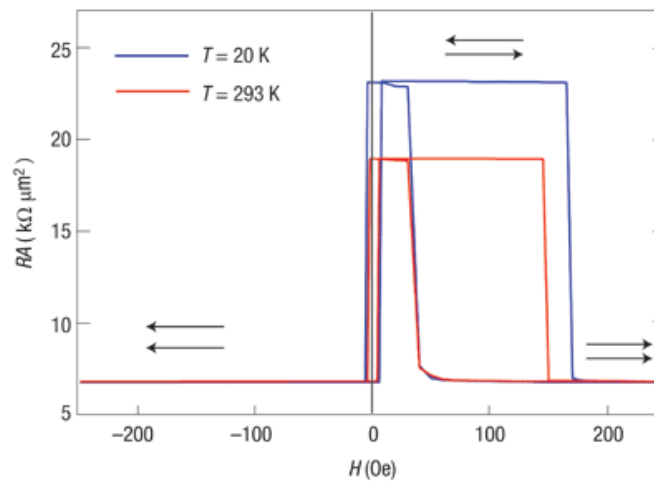


Figure 1.6 Illustration of a TMR signal[20]

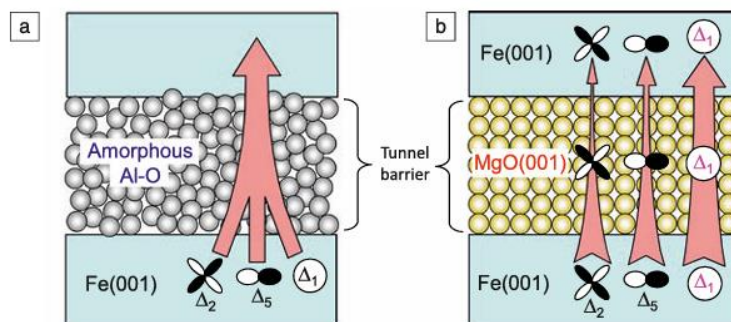


Figure 1.7 A schematic of (a) incoherent tunneling in amorphous Al-O barrier and (b) coherent tunneling dominated by Δ_1 in Fe/MgO/Fe structure[18]



1.3 Hall Effect

1.3.1 Anomalous Hall Effect (AHE)

The anomalous Hall effect (AHE) roots from the traditional Hall effect (HE), proposed by E. H. Hall in 1879, which depicts the transportation phenomenon of electrons under external magnetic field, as shown in Figure 1.8(a)[21]. In his theory, current-carrying charges will be “pressed” to a side by Lorentz force and deviate toward a transverse direction. Soon later in 1881, he proposed AHE, reporting that the same phenomenon is ten times larger in ferromagnetic irons, as shown in Figure 1.8(c)[22]. AHE signal provides an easy method to distinguish whether a solid contains ferromagnetic material or not.

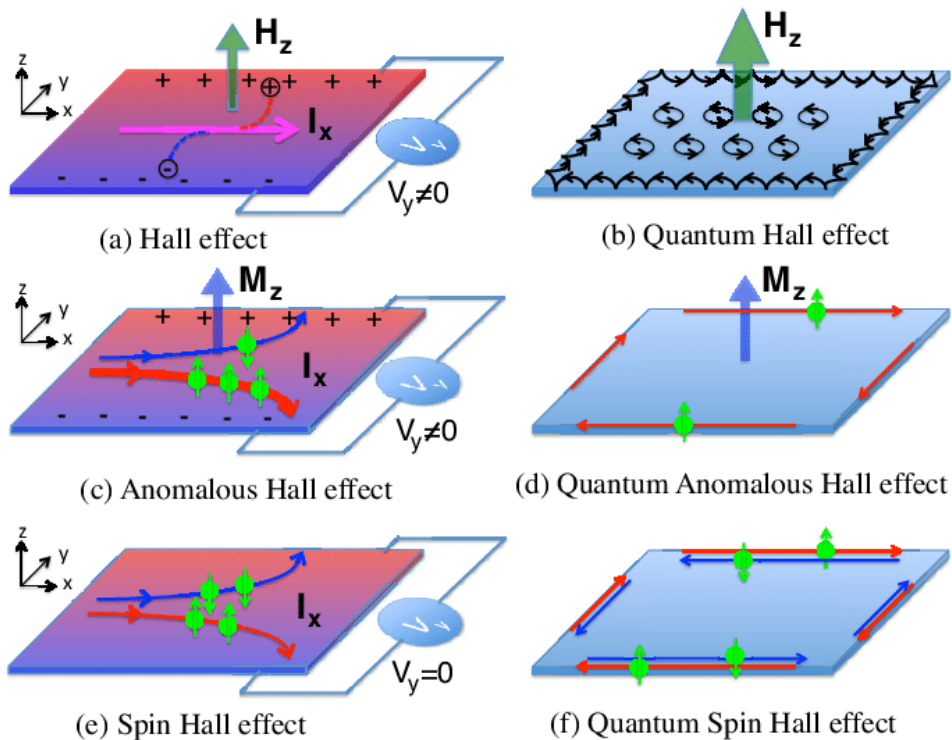


Figure 1.8 The Hall effect family[23]



1.3.2 Spin Hall Effect (SHE)

SHE was theoretically proposed by M. I. Dyakonov and V. I. Perel in 1971[24], and experimentally demonstrated by Y. Kato and J. Wunderlich in 2004 and 2005[25, 26]. Different from the FM materials in AHE, SHE depicts the transport phenomenon of electrons in heavy metal (HM) materials, e.g. Ta or W. When a charge current (J_c) flows into HM, it generates spin current (J_s) due to spin-orbit interaction, as shown in Figure 1.8(e)[27]. Typically, J_c is in x direction, the generated J_s is in the z direction and the spin polarization is in the y direction.

SHE provides a crucial method to manipulate the free layer in SOT MTJ structures, which will be further discussed in Chapter 1.4.1 and Chapter 1.4.2. HE, AHE and SHE are also crucial origins of the quantum Hall effects in Figure 1.8(b)(d)(f), when the materials are in strong magnetic fields.

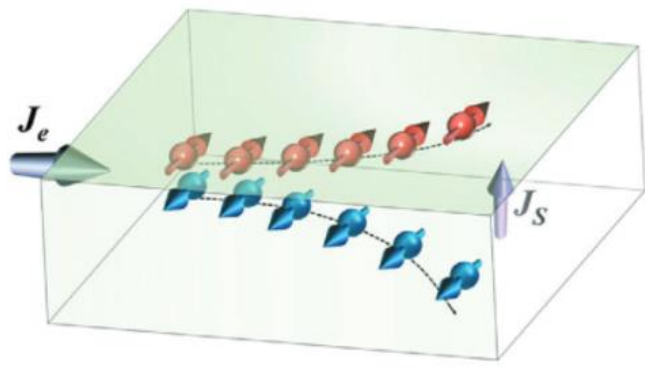


Figure 1.9 With spin Hall effect, incoming charge current can be converted into spin current.[28]

1.4 Magnetic Tunnel Junctions (MTJ)

1.4.1 Spin-Transfer Torque (STT) MTJ

STT MTJ and SOT MTJ refers to different types of manipulation methods. The

mechanism of STT MTJ was first theoretically predicted by Berger and Slonczewski in 1996[29, 30], and later experimentally demonstrated in 2004[31]. A common STT MTJ is shown as Figure 1.8, based on TMR effect. The two FM layers usually have different H_c . The one with smaller H_c can be called free layer (FL). The one with larger H_c can be called reference layer (RL) or fix layer.

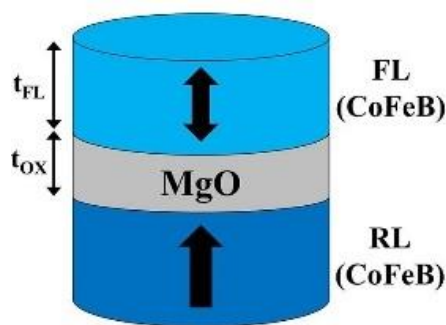


Figure 1.10 Schematic of an STT MTJ[32]

Since STT MTJ usually consists of two FM layers, we could detect these two layers by scanning an external field over its easy axis, as shown in Figure 1.11. The minor loop denotes the switching of the free layer, switching at a smaller H_c . The major loop denotes the switching of the reference layer. This switching can also be induced by applying current.

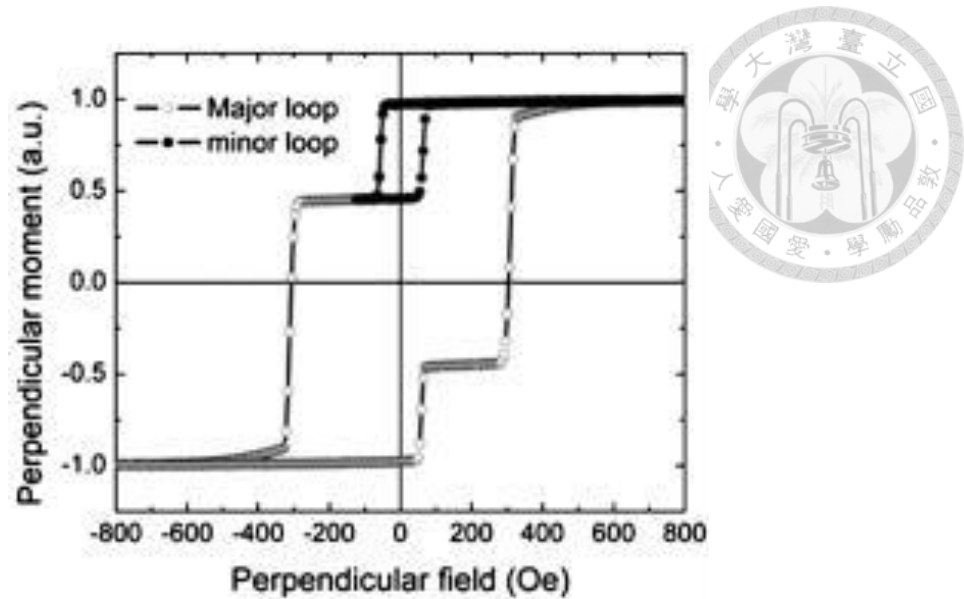


Figure 1.11 Illustration of a double loop signal and a minor loop[33]

1.4.2 Spin-Orbit Torque (SOT) MTJ

SOT MTJ is a modification of STT MTJ. Different from STT MTJ, the spin source of SOT MTJ is provided by SHE, as shown in Figure 1.12. Since the writing current is large in STT MTJ and sometimes leads to breakdown of MgO barrier, SOT MTJ is proposed to enhance the endurance[34]. The SOT channel is typically a HM layer, e.g. Ta, W, Pt and etc.[35, 36], due to their strong spin-orbit coupling effects. Among these materials, we use W as our SOT channel.

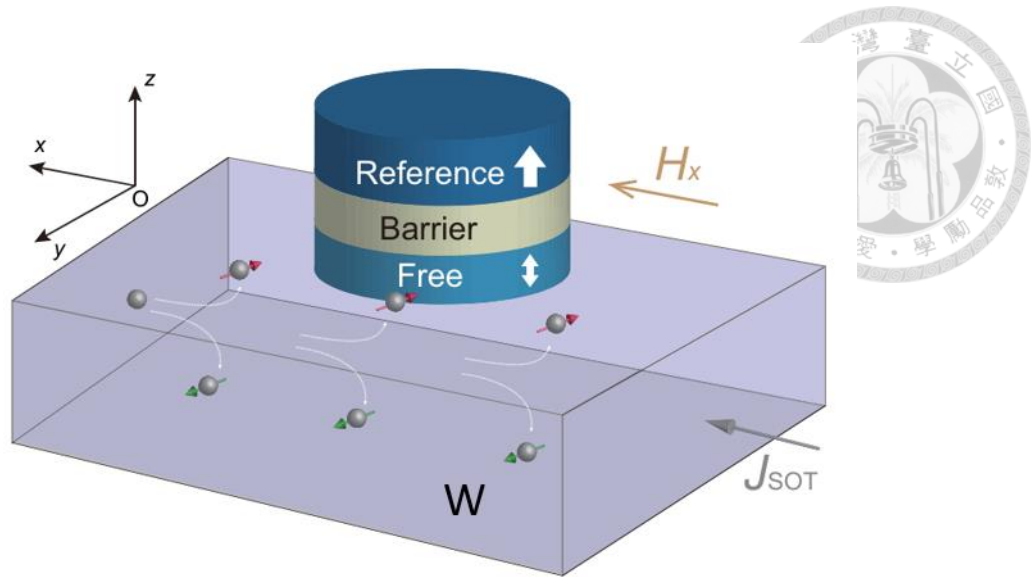


Figure 1.12 Schematic of an SOT MTJ with W, as its spin source layer[37]

1.4.3 Resistance Area (RA) product

It is demonstrated in different structures, including Fe/MgO/Fe and Fe/Al₂O₃, that $\log(RA)$ is proportional to t_{MgO} , as shown in Figure 1.13[20, 38]. According to the Wenzel-Kramer-Brillouin (WKB) approximation, the slope of $\log(RA)$ and t_{MgO} is $4\pi(2m\phi)^{1/2}/h$, where m , ϕ and h are, respectively, the electron mass, the potential barrier height and the Planck's constant[39].

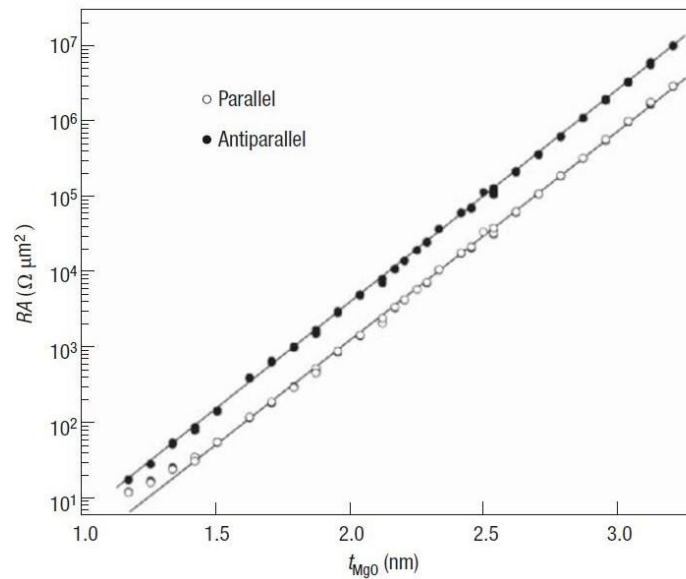


Figure 1.13 RA product shows an exponential trend to MgO thickness.[20]

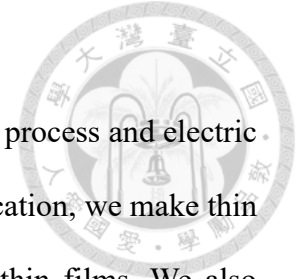
1.5 Motivation

To sum up the history and development of MTJ, different mechanism and physical structures, e.g. TMR, SHE and SOT MTJ, have been proposed to enhance the performance and make it more practical to integrate MTJ into other devices. The high TMR ratio provides clear signal change between P and AP state; the SHE and three-terminal SOT MTJ structure together reduces the chances of writing current to pass the thorough MTJ, which enhances the durability.

In order to acquire better control of these fundamental effects and mechanisms, modulation of MTJ thin films plays a crucial role. Upon modulating MTJ thin films, we demonstrate the application of TMR effect by MOKE detection, attain good control of H_c and collect different magnetic properties, including annealing time, angle dependence and etc., on the two FM layers, the free layer and the fix layer[6, 40, 41]. With these information, better control on switching states of MTJ could be achieved, and will be

helpful for further application[42, 43].

Furthermore, we also demonstrate a possible device fabrication process and electric detection of the three-terminal SOT MTJ devices. With device fabrication, we make thin films detectable by electric signals, rather than optical signal on thin films. We also perform different etching processes, e.g. stop-on-W and stop-on-MgO[44, 45].



Chapter 2 Sample Preparation



2.1 Thin Film Deposition

2.1.1 Magnetron Sputtering and Annealing

We use magnetron sputtering to grow thin films. Magnetron sputtering is a type of physical vapor deposition (PVD). The principle of magnetron sputtering lies in using plasma to bombard the target surface. These bombarded target fragments may condense on the anode substrate as a thin film. After growing the thorough thin film, we anneal the thin film with 400°C for 20 minutes.

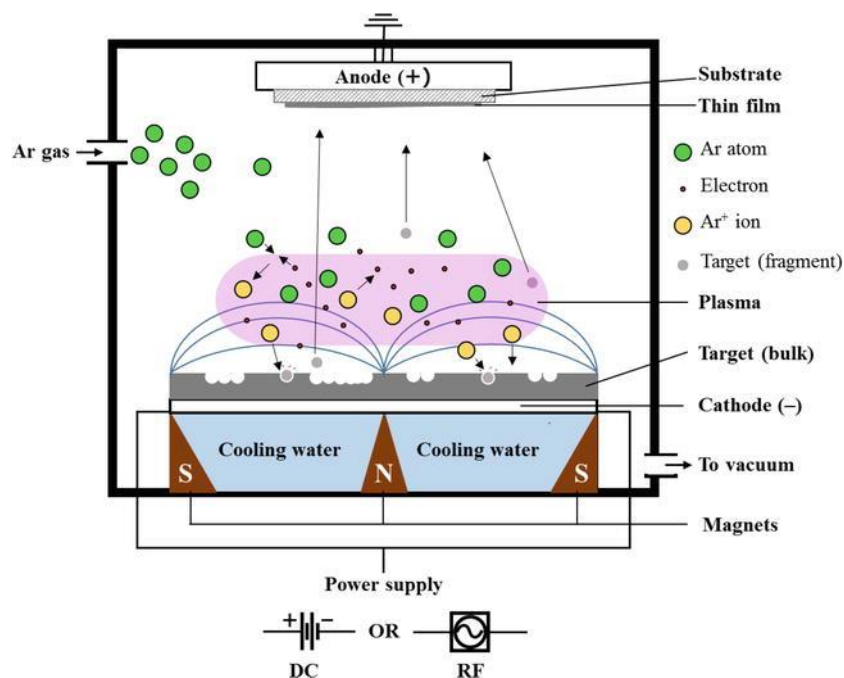


Figure 2.1 Illustration of magnetron sputtering[46]

2.2 Post Process for Device Manufacture



2.2.1 Photolithography

We use photolithography to define our device, pillar and electrode. Photolithography refers to step (2) to (5) in Figure 2.2. After photolithography, we then etch the sample and wash off the photoresist.

Our photolithography contains spin coating, soft baking, exposure and development. These four steps are conducted as followed. Firstly, photoresist is coated onto our sample. The photoresist is positive, which will be washed off after development. Secondly, the sample is soft baked for 100 seconds under 100°C. Thirdly, the sample with photoresist is exposed under UV light. Lastly, the sample develop will be developed by TMAH.

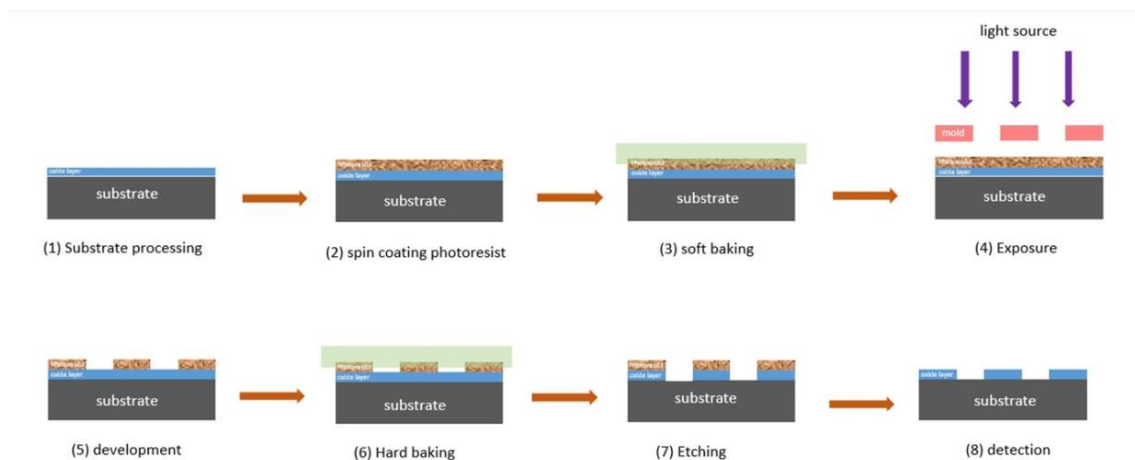


Figure 2.2 Common process of photolithography[47]

2.2.2 Ion Beam Etching (IBE)

Ion beam etching (IBE) is a type of physical etching. With IBE, we remove unwanted materials and transfer patterns onto our samples that are defined by mask and photoresist. IBE is preferred for etching stacks of multiple materials, e.g. MRAM, comparing to

complex chemical etching.

The setup of ion beam etching is as shown in Figure 2.3. There are three parts in IBE, including discharge chamber, the grids and the neutralizer. Ion production is done in the discharge chamber by subjecting argon gas to an RF field. Free electrons are excited by the RF field and will ionize argon to form plasma, once they have enough energy. The grid is important for extraction and acceleration of ions to the required energy. The neutralizer balances the charge of the ions, which can reduce space-charge effects.

During the etching processes, the parameters I use are as followed: etching angle at 80 degree, rotary 12 rpm. The etching time stops until the signal of desired materials (e.g. W or Mg) rises. The angle here is defined by the angle between the thin-film plane and the incident beam; that is, the ion beam is pointing nearly parallel to the plane normal. For the etching on second step, which will be specified in Chapter 2.3.1, we clean the sample at low angle afterwards. In this cleaning process, the parameters are: etching angle at 20 degree, rotary 30 rpm, 10 seconds.

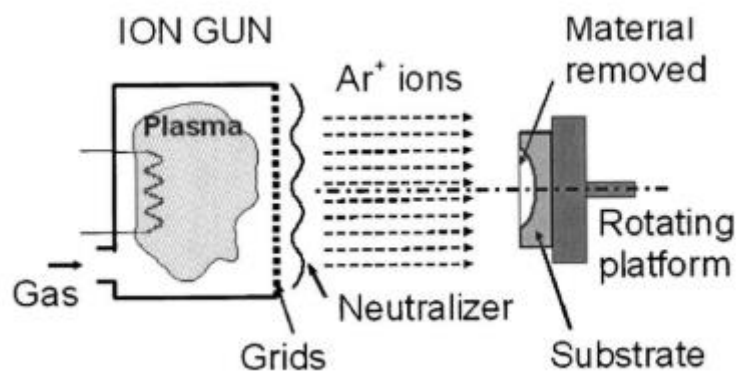


Figure 2.3 Schematic of ion beam etching[48]



2.2.3 Electron Beam Evaporator (EBE)

The setup of EBE is as shown in Figure 2.4. Similar to magnetron sputtering, EBE is a type of PVD. Instead of plasma, EBE uses accelerated electrons to bombard the target surface. The surface molecules will then be evaporated, travel toward the substrate and deposit as thin film. In our experiment, we use EBE to grow a 100 nm-thick SiO₂ layer.

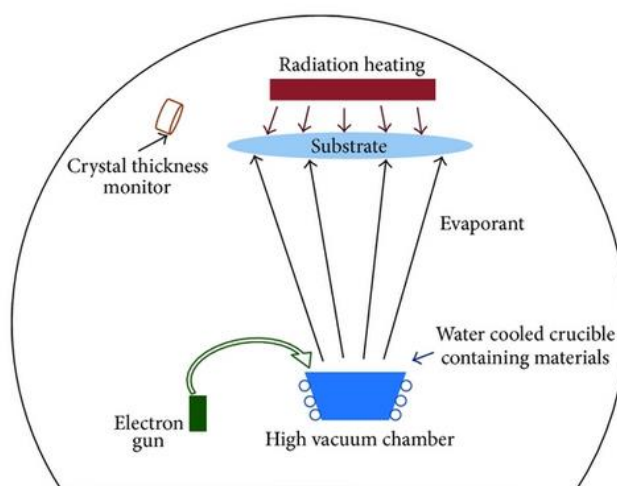


Figure 2.4 Illustration of E-beam evaporator[49]

2.3 Device Fabrication

2.3.1 MTJ Fabrication

The process of fabricating our device is as shown below.

In the first step, we define the device. We coat the photoresist onto the thin film and divide every device into two parts by lithography, which will later be top and bottom electrode. The details of photolithography are mentioned in Chapter 2.2.1. The mask pattern of this step is as shown in Figure 2.5(a) and the schematic is as shown in Figure 2.6(a). We then etch the thin film without covered photoresist as shown in Figure 2.6(b).

The parameters of etching are: etching angle at 80 degree, rotary 12 rpm. The angle here is defined by the angle between the thin-film plane and the incident beam. Afterwards, we use acetone and isopropyl alcohol (IPA) to strip off the photoresist, Figure 2.6(c).

In the second step, we define the pillar. Again, we transfer the pattern of the second mask Figure 2.5(b) onto the thin film with lithography and the schematic is as shown in Figure 2.6(d). We then etch the pillar until W or MgO as shown in Figure 2.6(e)[44, 45]. After the second etching, I perform cleaning to the sample. The parameters of cleaning are: etching angle at 20 degree, rotary 30 rpm, 10 seconds. Apart from the first step, we grow 100-nm-thick SiO₂ as in Figure 2.6(f). Afterwards, we use acetone and IPA again to strip off the photoresist, Figure 2.6(g).

In the third step, we define the top electrode. This “top” electrode refers to the top of the pillar as in Figure 2.6(h). Likewise, “bottom” refers to the bottom of the pillar. The mask of the third lithography is shown in Figure 2.5(c). We deposit Ta(9nm)/W(90nm) as electrode atop of pillar.

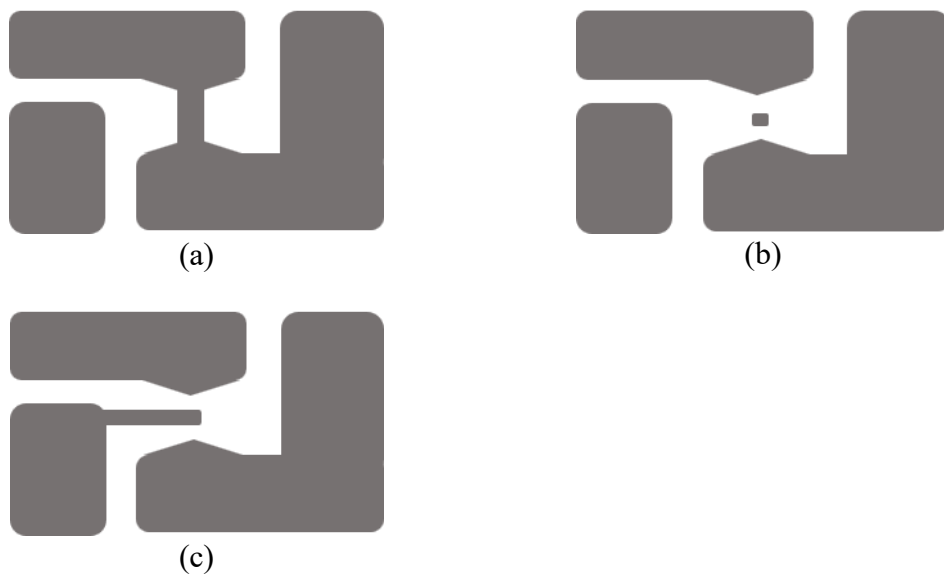
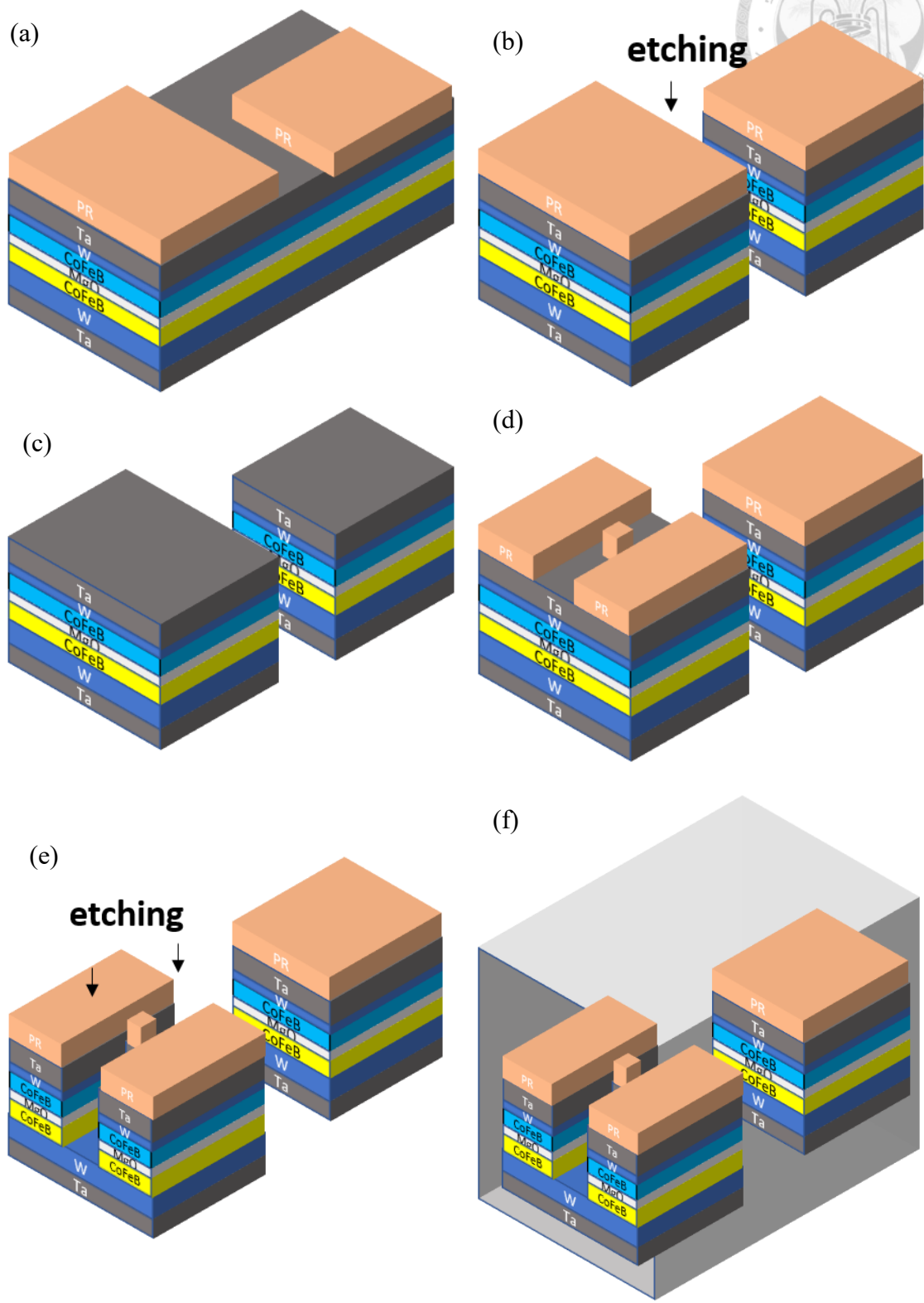


Figure 2.5 Mask patterns of different MTJ fabrication steps (a) 1st lithography (b) 2nd lithography (c) 3rd lithography



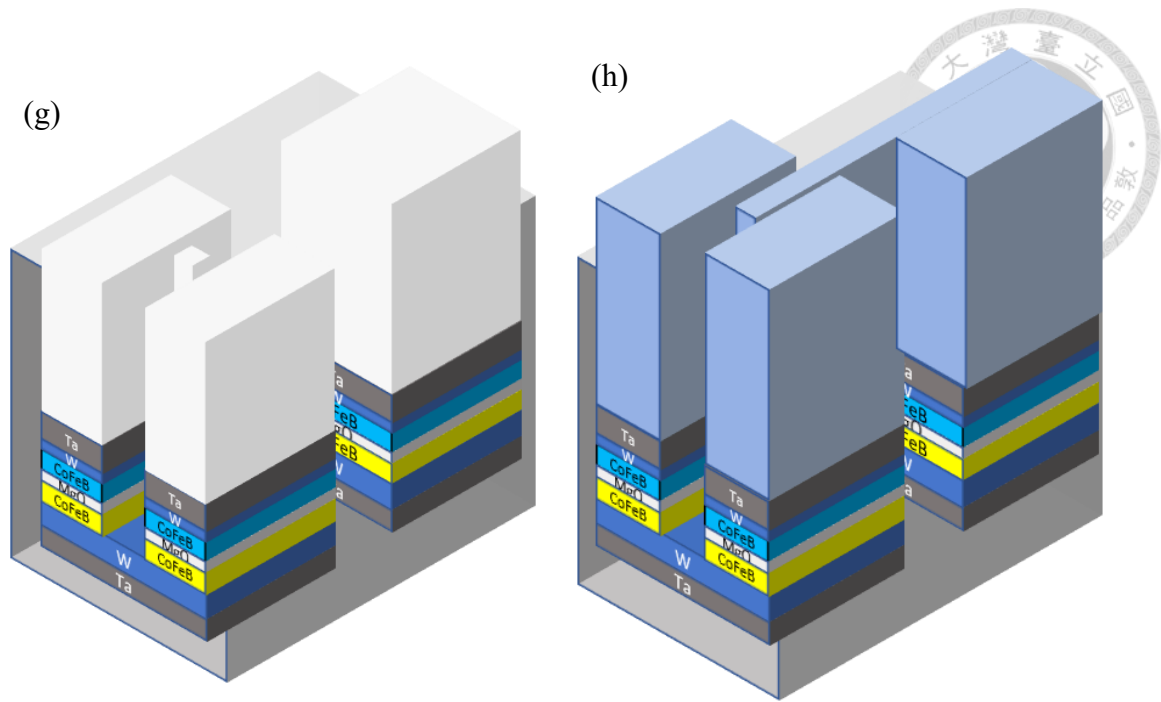


Figure 2.6 Schematic of different MTJ fabrication steps (a) 1st lithography (b) 1st etching (c) thin film after 1st process (d) 2nd lithography (e) 2nd etching (f) E-gun evaporation by SiO₂ (g) thin film after 2nd process (h) 3rd lithography and electrode

Since we fabricate 30 devices at a time, the arrangement of these devices is as shown in Figure 2.7 and Table 2.1. We define the pillar size as $(a \times b) \mu\text{m}^2$. Side “a” ranges from 2 to 12 while side “b” from 2 to 10, both of them are counted by twos. Thus, we get 30 devices.

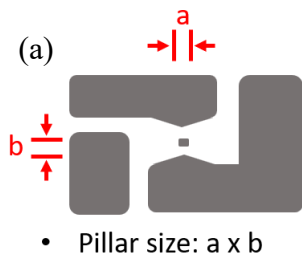


Figure 2.7 (a) The definition of pillar size (b) The arrangement of 30 devices

2x2	2x4	2x6	2x8	2x10
4x2	4x4	4x6	4x8	4x10
6x2	6x4	6x6	6x8	6x10
8x2	8x4	8x6	8x8	8x10
10x2	10x4	10x6	10x8	10x10
12x2	12x4	12x6	12x8	12x10

Table 2.1 The devices are arranged based on their pillar sizes as Figure 2.7.

Chapter 3 Measurement



3.1 Thin Film Measurement

3.1.1 Magneto-Optical Effect (MOKE)

The Magneto-Optical effect (MOKE) brings out the change of magnetization by using the change in polarization of light. Based on its geometry, MOKE can be categorized into three modes, as shown in Figure 3.1. We use (a) Polar and (b) Longitudinal mode in our experiments, on detecting samples with out-of-plane and in-plane magnetization respectively. This method provides a fast and harmless measurement on detecting thin film magnetization.

The setup of polarizer and analyzer is as shown in Figure 3.2. Both polarizer and analyzer are polarizing filters arranged in different angles. They are sheets that transmit only the component of light polarized along the transmission axis. The polarization of light changes, as it goes through the sequence of polarizer, sample, analyzer, and the detector. The natural light is not polarized at first. After passing the polarizer, the light become linear. This outgoing beam then hits the magnetic sample and undergoes some change in polarization. The analyzer is placed in a near extinction, which the light can barely pass without the change in sample. Finally, the signal is collected by a detector that gives its voltage.

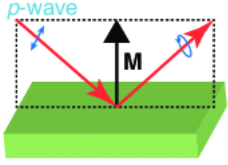
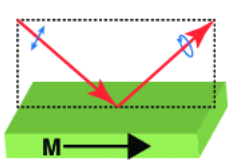
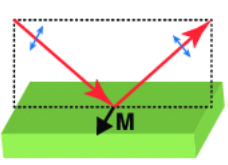
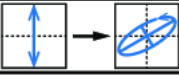

Name	(a) Polar	(b) Longitudinal	(c) Transverse
Geometry			
Detection	Out-of-plane	in-plane	in-plane
Polarization Variation	Rotation Ellipticity		None 
Measurement	Polarization Analysis		Intensity measurement

Figure 3.1 Three geometries of MOKE includes (a) Polar (b) Longitudinal and (c) Transverse.[50]

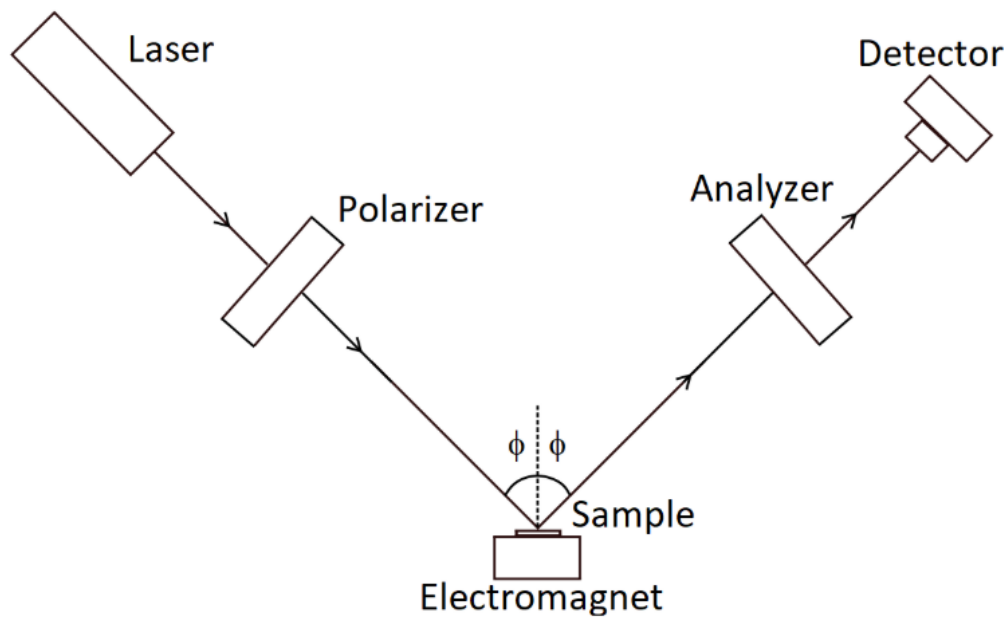


Figure 3.2 Schematic of MOKE setup[51]

3.2 Secondary Ion Mass Spectrometry (SIMS)

SIMS is a powerful chemical characterization technique, detecting secondary ions with a mass spectrometer. In our experiment, SIMS detection is carried out during etching,

which determines where to stop on a specific layer.

The setup of SIMS detection is shown as Figure 3.3. During etching, there are some secondary ions ejected by high energy. These ions will be guided toward the detector with an applied electric field, and recognized by their mass-to-charge ratio with mass spectrometry. As the etching process goes, SIMS provides a real-time signal as shown in Figure 3.4, with a good end point resolution of $\pm 5\text{\AA}$.

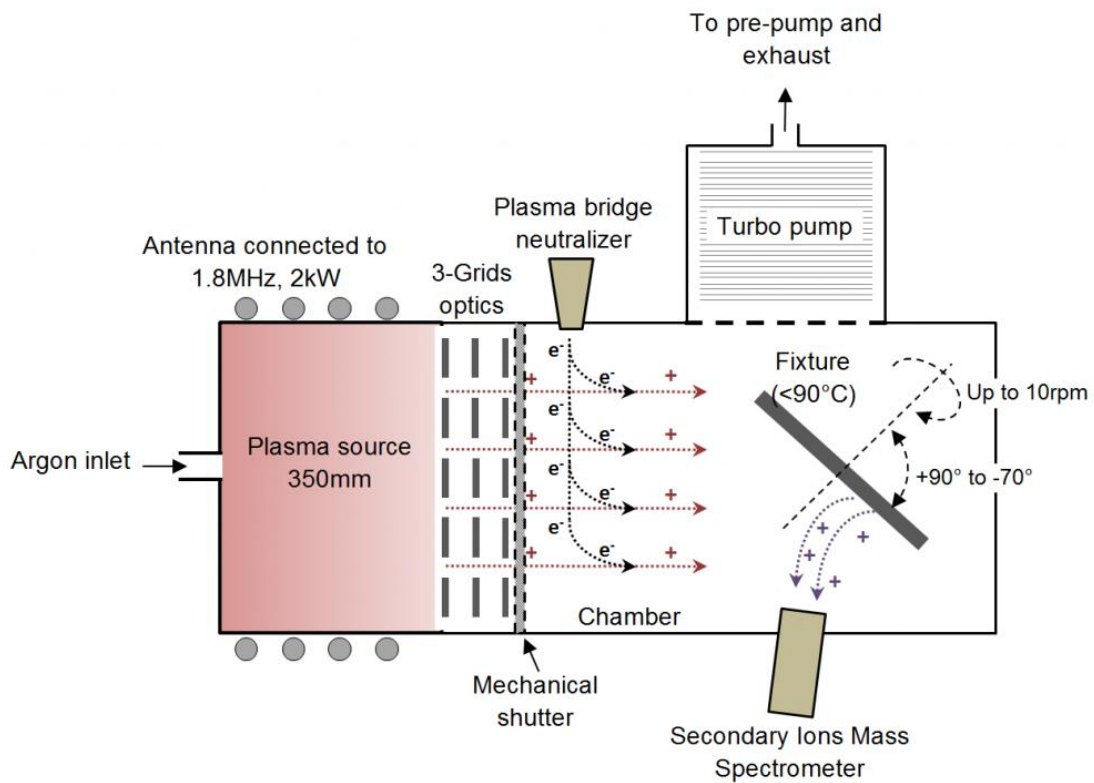


Figure 3.3 Schematic of SIMS detection during IBE[52]

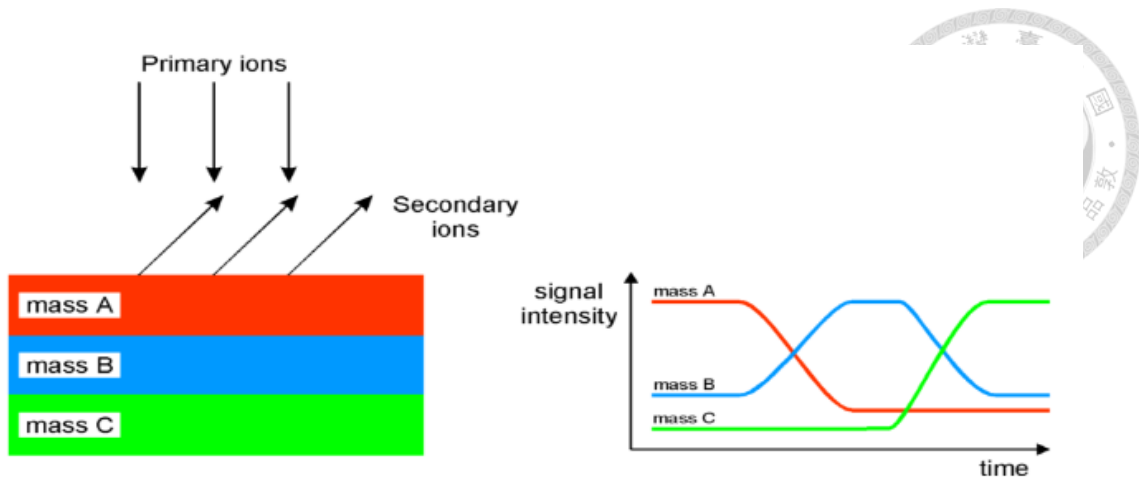


Figure 3.4 SIMS provides real-time signal during etching[52]

3.3 MTJ Measurement

3.3.1 TMR Measurement

An illustration of TMR measurement is shown below in Figure 3.5. The green line denotes the current between top electrode and bottom electrode, which will be referred to as “top-to-bottom”. The red line denotes current between two bottom electrodes, and will be referred to as “bottom-to-bottom”. Based on the TMR effect mentioned in Chapter 1.2.2, we can detect TMR signal by measuring the resistance.

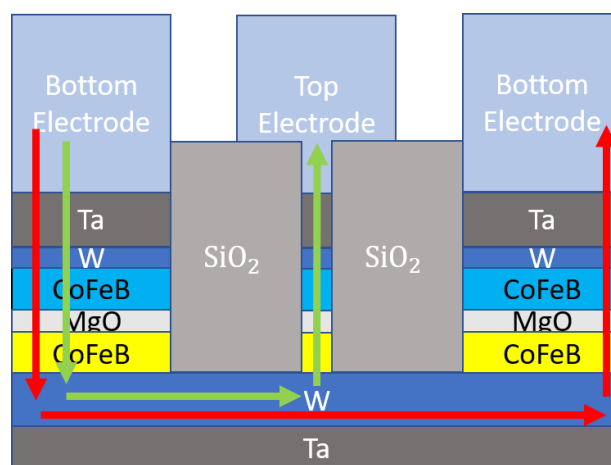


Figure 3.5 Schematic of current flow during TMR measurement

Chapter 4 Results and Discussion



4.1 PMA Thin Film

4.1.1 Half MTJ Structure

In order to fabricate an MTJ, the first goal is to form a double loop as Figure 1.11. This double loop can be differentiated into PMA thin films and IMA thin films as in Chapter 1.1.2, which differs in their direction of magnetization. I will focus first on PMA thin films, and will discuss IMA thin films later in Chapter 4.2.

We start with half structure; the bottom half is Ta/W/CFB/MgO/Ta and the top half is MgO/CFB/W/Ta. From previous studies, we learned that the bottom and top structures have different interfacial dead layer[6, 40] and different thickness range to achieve PMA[41]. Therefore, we try to get smallest H_c of bottom half structure and largest H_c of top half structure, by modulating thickness of different layers. It will be helpful since they will be free and fix layer respectively after combination.

We modulate the CoFeB thickness of the two structures. In Figure 4.1(a), we deposit a Ta(2)/W(4)/CFB(t)/MgO(1.5)/Ta(4) structure, where $t = 1.0, 1.2, 1.4, 1.6, 1.8, 2.0, 2.2$. Among all thicknesses, we find CoFeB(1.6) to be the best thickness in the bottom half structure. (The thickness here and later will all be measured in nm scale.) In Figure 4.1(b), we deposit a MgO(1.5)/CFB(t)/W(0.5)/Ta(4) structure, where $t = 1.4, 1.6, 1.8, 2.0, 2.2, 2.4, 2.6, 2.8$. Among all thicknesses, we find largest H_c when CoFeB thickness is between 1.6nm and 2.0nm.

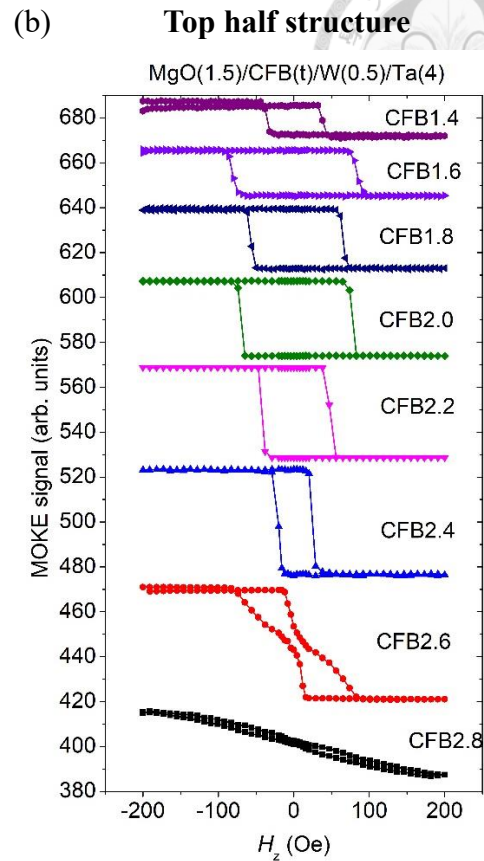
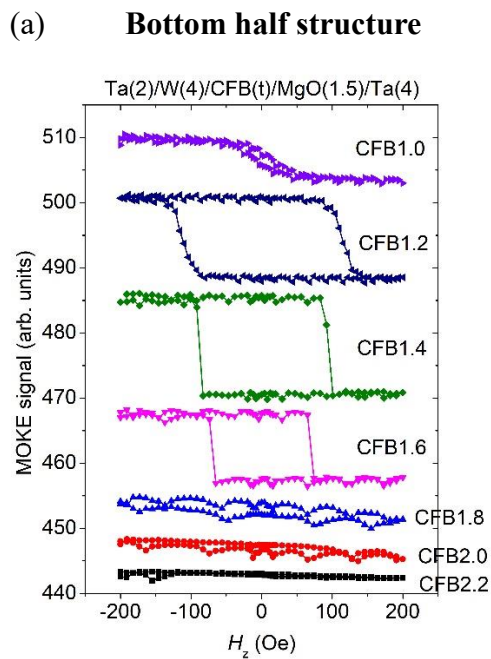


Figure 4.1 (a) Among all thicknesses with good hysteresis loop, CFB(1.6) shows the smallest H_c . (b) For $1.6 \leq t_{CFB} \leq 2.0$ nm, it shows the largest H_c .

4.1.2 Full MTJ Structure

After we find the optimized structure of each half, we combine the two half structures into a full structure. In Figure 4.2, we deposit Ta(2)/W(4)/CFB(1.6)/MgO(1.5)/CFB(t)/W(0.5)/Ta(4), where $t = 1.6, 1.7, 1.8, 1.9$. However, we don't see any double loops as expected at first.

Since modulating CoFeB thickness doesn't provide double loop, we modulate MgO thickness. In Figure 4.3, we deposit Ta(2)/W(4)/CFB(1.6)/MgO(t)/CFB(2.0)/W(0.5)/Ta(4), where $t = 1.2, 1.3, 1.4, 1.5, 1.6, 1.7, 1.8$. However, this doesn't provide

evident double loop either.

We then modulate W thickness. In Figure 4.4, we change W thickness from 0.5nm to 0.7nm, and deposit Ta(2)/W(4)/CFB(1.6)/MgO(1.2)/CFB(2.0)/W(0.7)/Ta(4). It then shows double loop.

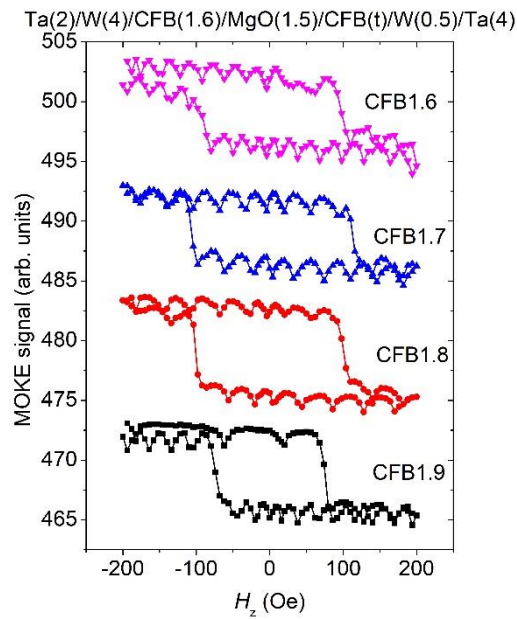
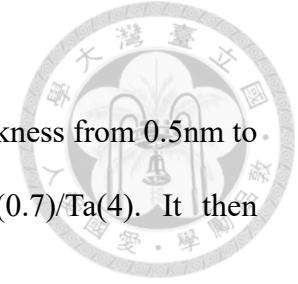


Figure 4.2 It doesn't show double loop after combining two half layers into a full MTJ structure, with fix layer CFB thickness from 1.6 to 2.0.

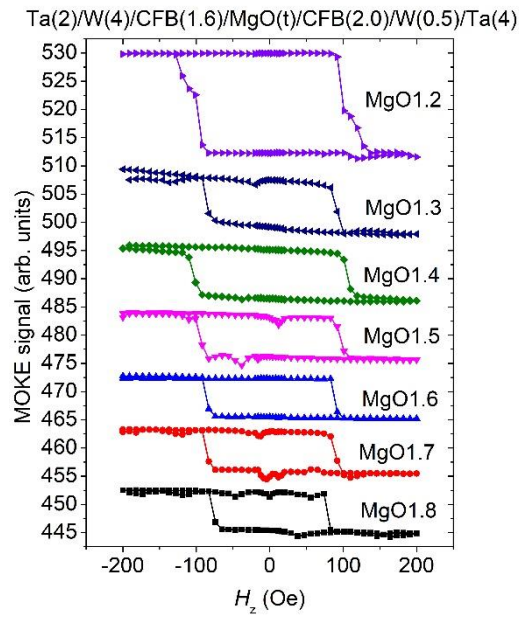


Figure 4.3 Since it doesn't show double loop after modulating CFB thickness, we therefore modulate MgO thickness.

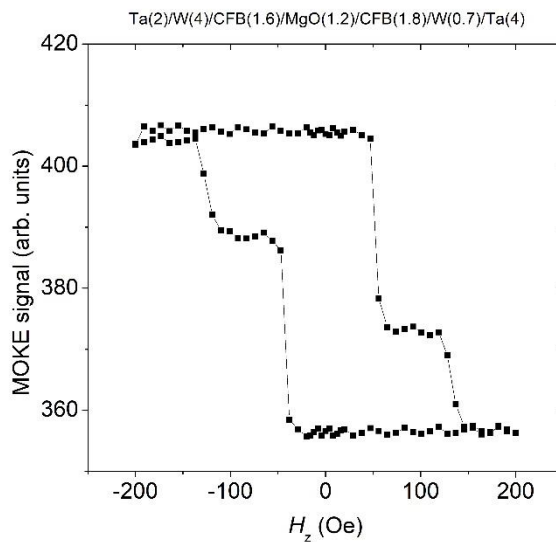


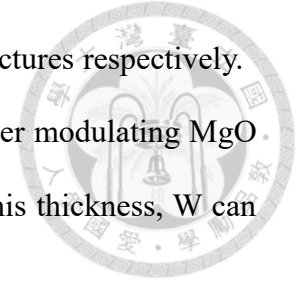
Figure 4.4 It shows double loop after modulating W thickness.

4.1.3 Short Conclusion

For half MTJ structure, we can easily determine the best thickness with appropriate

H_c . In this case, CFB(1.6) and CFB(2.0) for bottom and top half structures respectively.

For full MTJ structure, it doesn't show double loop at first, after modulating MgO thickness. It shows double loop after modulating W thickness. At this thickness, W can stop Ta diffusion into CFB layer.



4.2 IMA Thin Film Annealed without External Field

4.2.1 Half MTJ Structure

Similar to PMA MTJ, we modulate IMA MTJ from its half structure. For bottom half MTJ, Figure 4.5(a), we deposit a Ta(2)/W(4)/CFB(t)/MgO(1.5)/Ta(4) structure, where $t = 2.0, 2.5, 3.0, 3.5, 4.0, 4.5$. It's worth noticing that the CoFeB thicknesses here are much thicker than PMA thin films, due to higher contribution of bulk anisotropy in Chapter 1.1.2. Among all thicknesses, CFB(3) shows the smallest H_c . For top half MTJ, Figure 4.5(b), we deposit a MgO(1.5)/CFB(t)/W(0.5)/Ta(4) structure, where $t = 3.0, 3.5, 4.0, 4.5, 5.0, 5.5$. H_c are large enough for CoFeB thicker than 4nm.

In Figure 4.6, we measure the hysteresis loop of these bottom and top half structures, the same structures in Figure 4.5. As shown in the figure, as-deposited samples show smaller H_c . We extract H_c of these different thicknesses and make it into Figure 4.7.

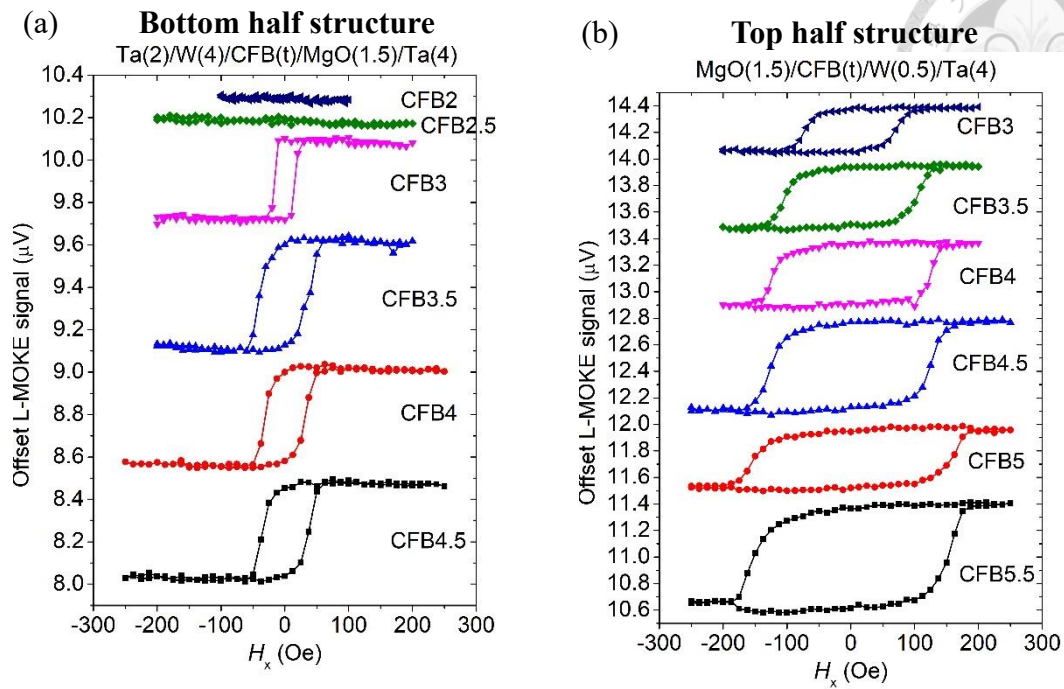


Figure 4.5 (a) CFB(3) shows the smallest H_c . (b) H_c are large enough for CFB thicker than 4nm.

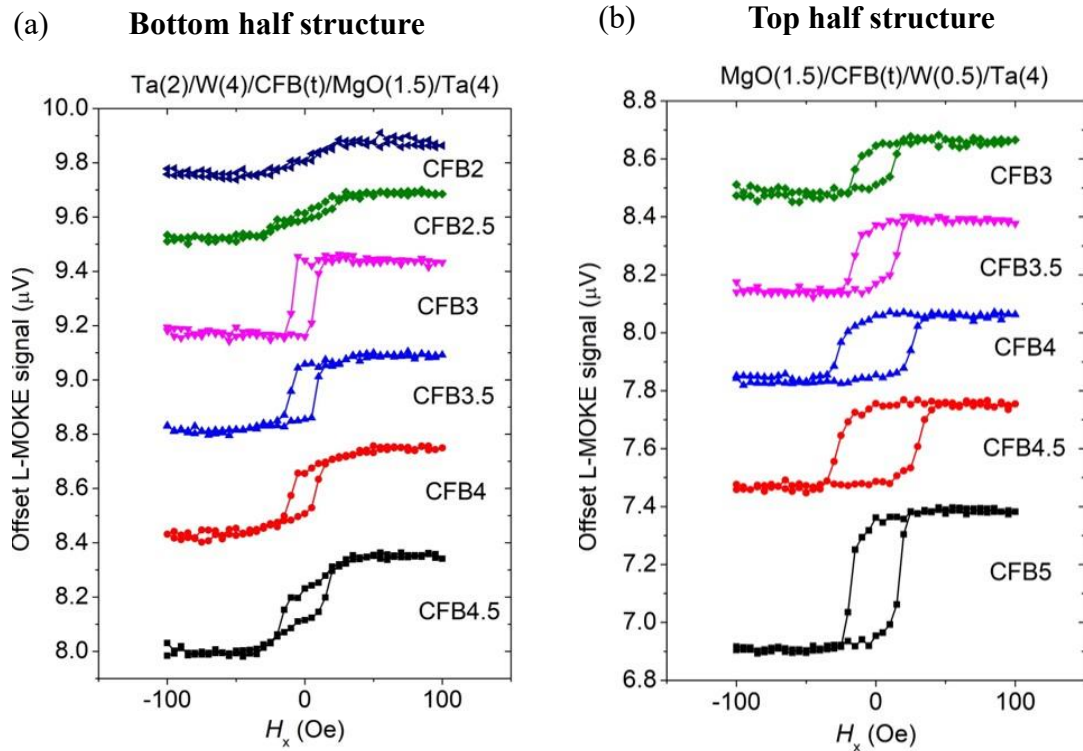


Figure 4.6 (a)(b) As-deposited thin films show smaller H_c . These thin films are the same structures as in Figure 4.5.

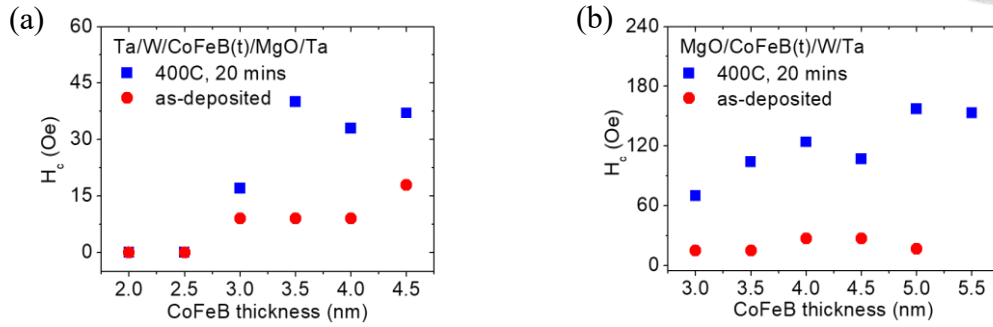
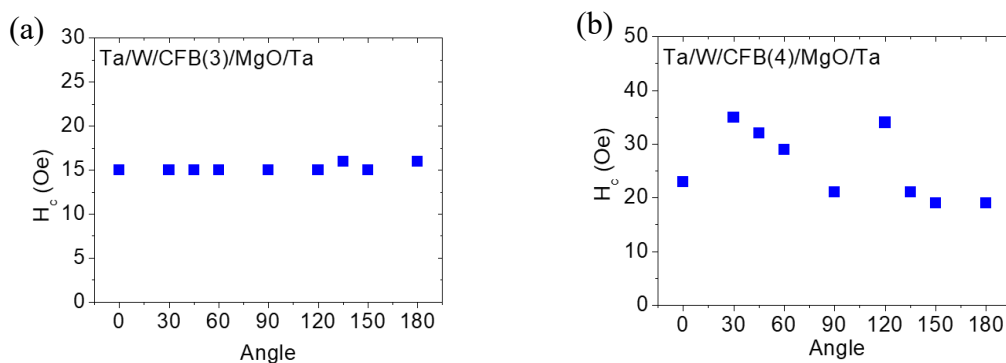


Figure 4.7 H_c extracted from Figure 4.5 and Figure 4.6. (a)(b) After annealing, coercivity significantly increases.

Since the sample are IMA, we further investigate its behavior on xy-plane. We measure the hysteresis loops of bottom half structures, Ta(2)/W(4)/CFB(t)/MgO(1.5)/Ta(4) structure, where $t = 3.0, 4.0, 4.5$, and extract their H_c into Figure 4.8. In Figure 4.8(a), CFB(3), H_c doesn't fluctuate at different angle. In Figure 4.8(b)(c), although H_c fluctuates at different angle, there are no evident regulation.



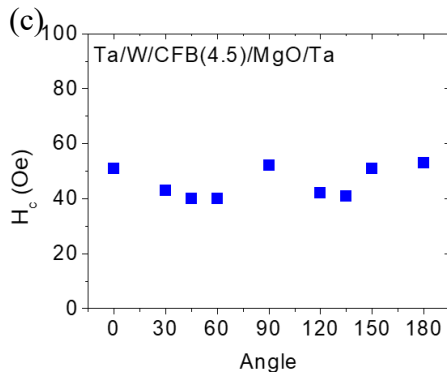


Figure 4.8 H_c extracted from Figure 4.7. (a) For CFB(3), no angle dependence is observed. (b)(c) For CFB(4) and (4.5), although H_c fluctuates at different angle, there are no evident regulation.

4.2.2 Full MTJ Structure

Similar to PMA thin films, we combine the two half structures into full structure. In Figure 4.9, we deposit Ta(2)/W(4)/CFB(3)/MgO(1.5)/CFB(t)/W(0.5)/Ta(4), where $t = 3.5, 4, 4.5$, and Ta(2)/W(4)/CFB(3.5)/MgO(1.5)/CFB(t)/W(0.5)/Ta(4), where $t = 3.5, 4, 4.5$. However, it doesn't show double loop at first when we modulate free layer CoFeB thickness.

In Figure 4.10(a), we modulate MgO layer and deposit Ta(2)/W(4)/CFB(3)/MgO(t)/CFB(4)/W(1)/Ta(4), where $t = 1.2, 1.3, 1.4, 1.5, 1.6, 1.7, 1.8, 1.9$. Layers with MgO thickness between 1.2-1.5 nm and fix-CFB(4) starts to show evident double loops. In Figure 4.10(b), we change fix layer CFB thickness to 5nm, and deposit Ta(2)/W(4)/CFB(3)/MgO(t)/CFB(5)/W(1)/Ta(4), where $t = 1.0, 1.1, 1.2, 1.3, 1.4$.

In Figure 4.11, we deposit a thinner MgO layer with thickness at 1nm, and deposit Ta(2)/W(4)/CFB(3)/MgO(1)/CFB(t)/W(1)/Ta(4), where $t = 4.0, 4.2, 4.4, 4.6, 4.8, 5.0$. It shows double loops for fix-CFB thickness from 4–4.8 nm.

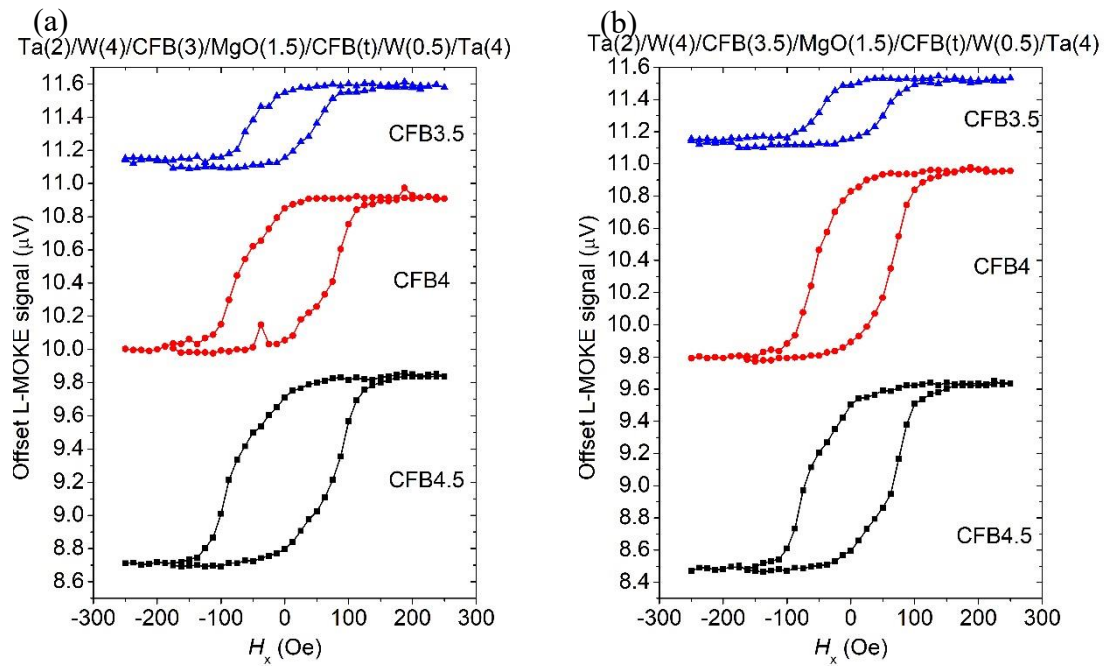


Figure 4.9 It doesn't show double loop for free-CFB(3) and free-CFB(3.5).

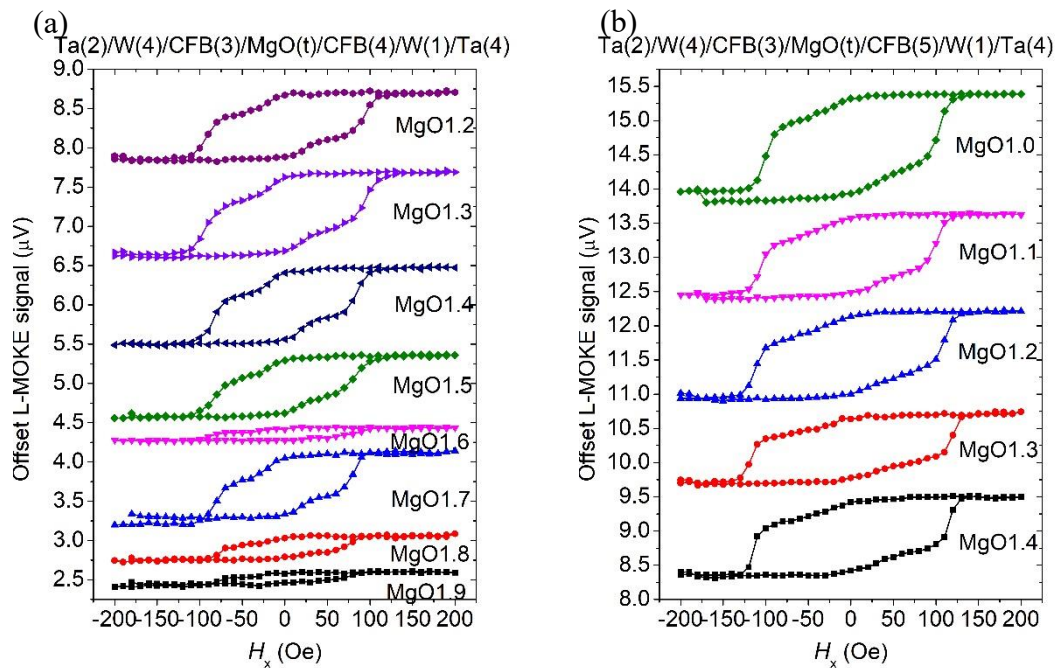


Figure 4.10 (a) After annealing, it shows double loops for $1.2 \leq t_{\text{MgO}} \leq 1.5$ nm for fix-CFB(4). (b) It does not show evident double loop for fix-CFB(5).

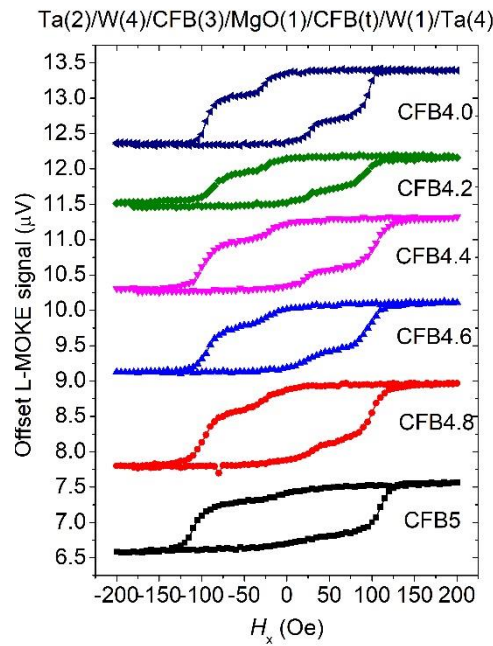


Figure 4.11 For thinner MgO thickness t_{MgO} (1), it shows double loops for fix-CFB thickness from 4–4.8 nm.

Based on the successful thin films above, we also modulate the annealing time. We deposit a series of Ta(2)/W(4)/CFB(3)/MgO(t)/CFB(4)/W(1)/Ta(4), where $t = 0.8, 0.9, 1.0, 1.1, 1.2, 1.3, 1.4, 1.5$, and anneal these structures for 20, 30, 40, 50 minutes, as shown in Figure 4.12 (a)(b)(c)(d), respectively. At all annealing time, there are some structures that show double loop. With longer annealing time, the double loops become sharper. However, the signal-to-noise ratio gets larger as well. In Figure 4.13, we scan the minor loop of the thin films in Figure 4.12.

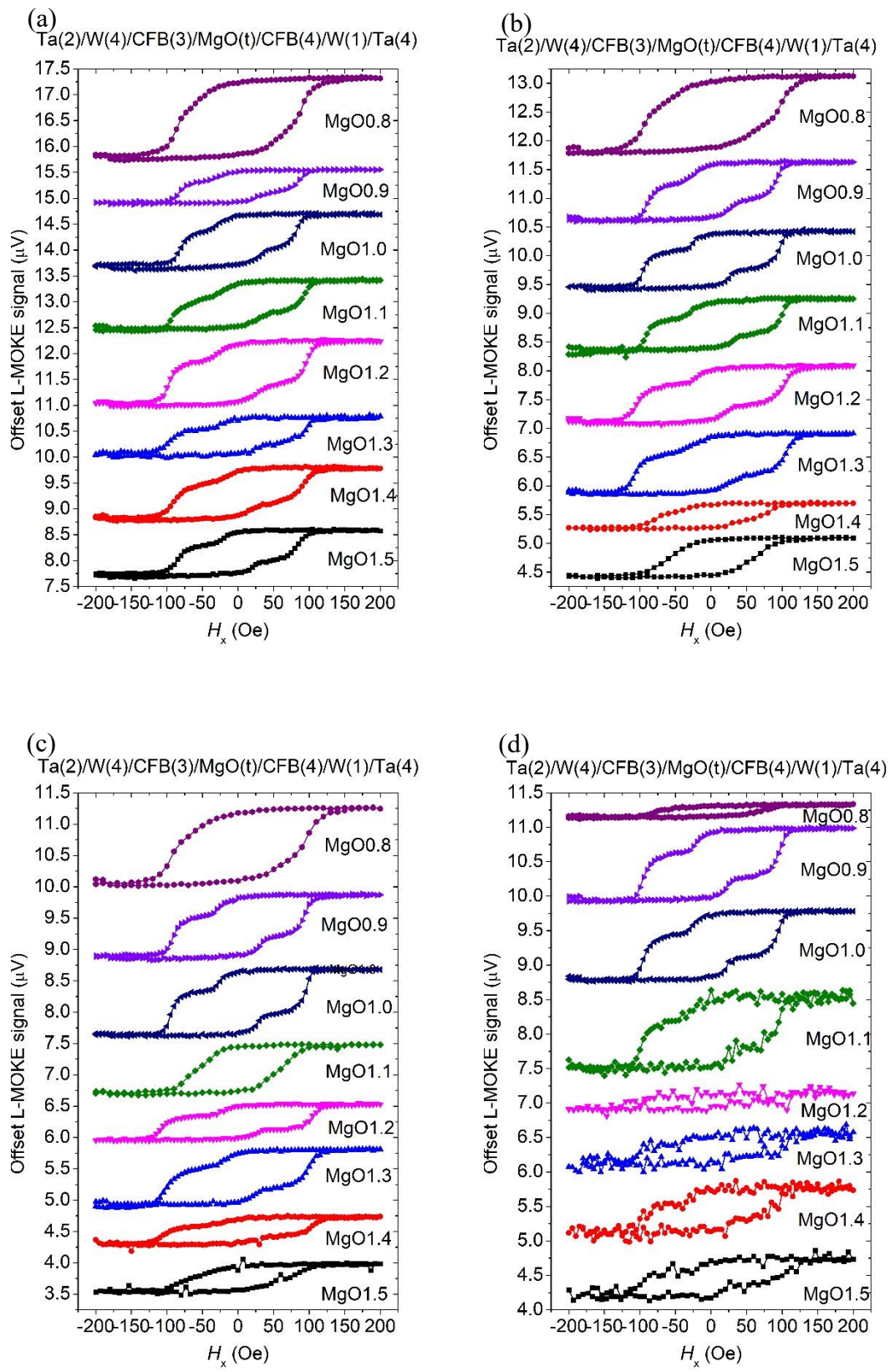


Figure 4.12 Samples are annealed for (a) 20 (b) 30 (c) 40 (d) 50 minutes. With longer

annealing time, the double loops become sharper.

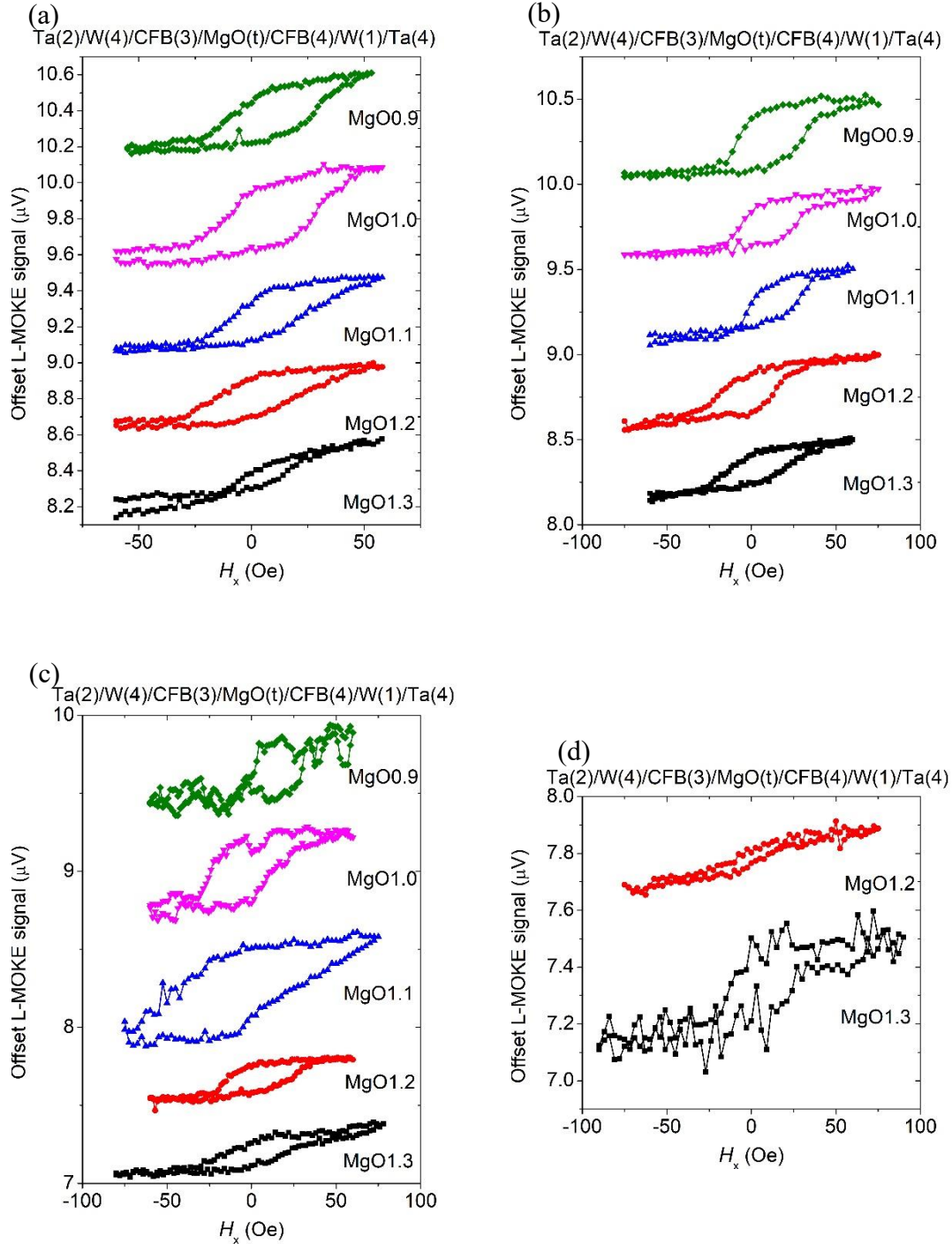


Figure 4.13 (a)(b)(c)(d) Minor loop of the same thin films in Figure 4.12.



4.2.3 Short Conclusion

For half MTJ structures, we find appropriate H_c for bottom half structure Ta(2)/W(4)/CFB(3)/MgO(1.5)/Ta(4), and for top half structures MgO(1.5)/CFB(t)/W(0.5)/Ta(4), where $t = 4.0, 4.5, 5.0, 5.5$. We also find that annealing can significantly increase coercivity, when comparing as-deposited thin films and annealed thin films. These thin films do not show obvious regulation of easy and hard axes.

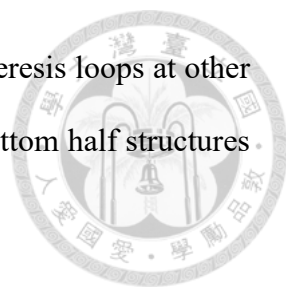
For full MTJ structure, we modulate fix layer CoFeB thickness and MgO thickness, and obtain double loop in the structure Ta(2)/W(4)/CFB(3)/MgO(t)/CFB(4)/W(1)/Ta(4), where $t = 1.2, 1.3, 1.4, 1.5$. When applying different annealing time to the thin films, 20, 30, 40, and 50 minutes, many thin films still show double loop. However, these double loops do not have easy and hard axes behaviors either. We also scan the minor loops of these thin films, and attain their behavior under smaller external field.

4.3 IMA Thin Film Annealed with External Field

4.3.1 Half MTJ Structure

As demonstrated in Chapter 4.1 and Chapter 4.2, we successfully modulated double loops for PMA and IMA thin films. However, in Figure 4.8, we demonstrated that there are no evident regulations at different angles for our IMA thin films. Therefore, we will anneal these modulated thin films with external field 8000 Oe, to see whether they show easy and hard axes behaviors.

Here, we select thin films with better H_c , Ta(2)/W(4)/CFB(3)/MgO(1.5)/Ta(4) and MgO(1.5)/CFB(4)/W(0.5)/Ta(4), for bottom and top half structures respectively. In Figure 4.14, bottom structures show easy and hard axes behaviors, while top structures



do not. With the hysteresis loops of Figure 4.14 and some other hysteresis loops at other angles, we extracted their H_c into Figure 4.15, we can see that the bottom half structures are strongly dependent on angle, while the top half structures are not.

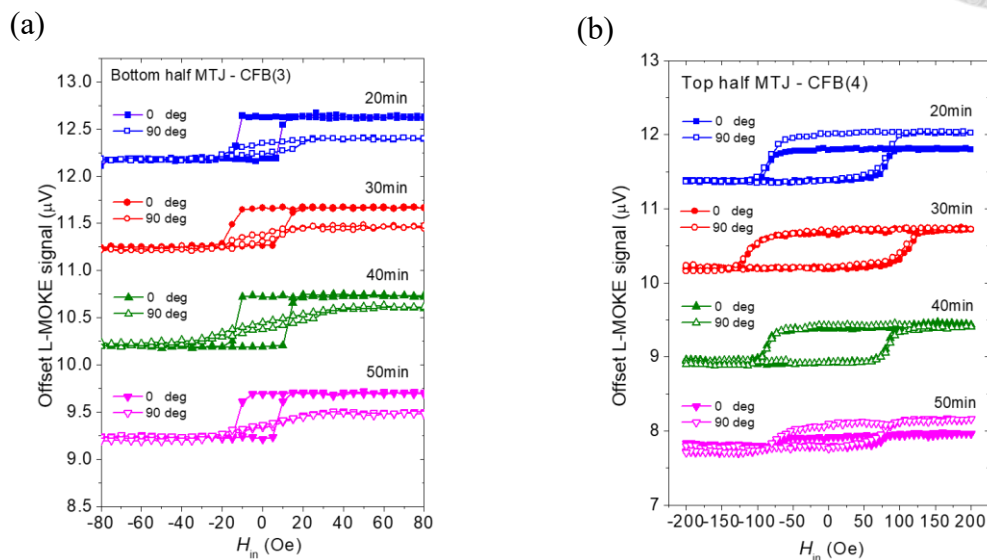


Figure 4.14 (a) For bottom half MTJ, easy and hard axis can be easily distinguished, but coercivity of easy axis does not increase after annealing with external field. (b) For top half MTJ, hysteresis loops don't show evident easy and hard axes behaviors after annealing.

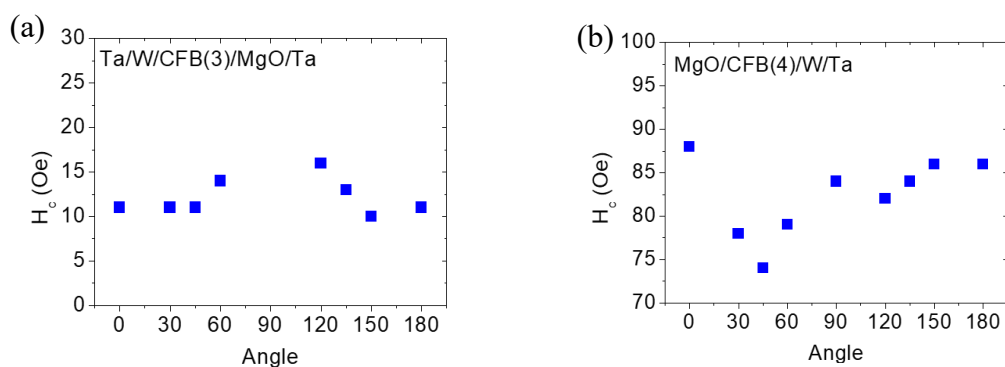


Figure 4.15 (a) For the extracted H_c of bottom half structure, the regulation of easy and hard axes are clearly shown. (b) For the top half of MTJ, the coercivity does not

have strong regulation to angle.



4.3.2 Full MTJ Structure

Although the top half structure didn't show evident hard and easy axes behaviors, we still select a full structure with double loops, from Figure 4.12(c), which is annealed for 40 minutes. We choose Ta(2)/W(4)/CFB(3)/MgO(t)/CFB(4)/W(1)/Ta(4), where $t = 0.9, 1.0$. For the two thin films, Ta(2)/W(4)/CFB(3)/MgO(0.9)/CFB(4)/W(1)/Ta(4) shows double loop, as shown in Figure 4.16.

In Figure 4.17, we compare their H_c with different annealing time. However, different annealing time doesn't change H_c .

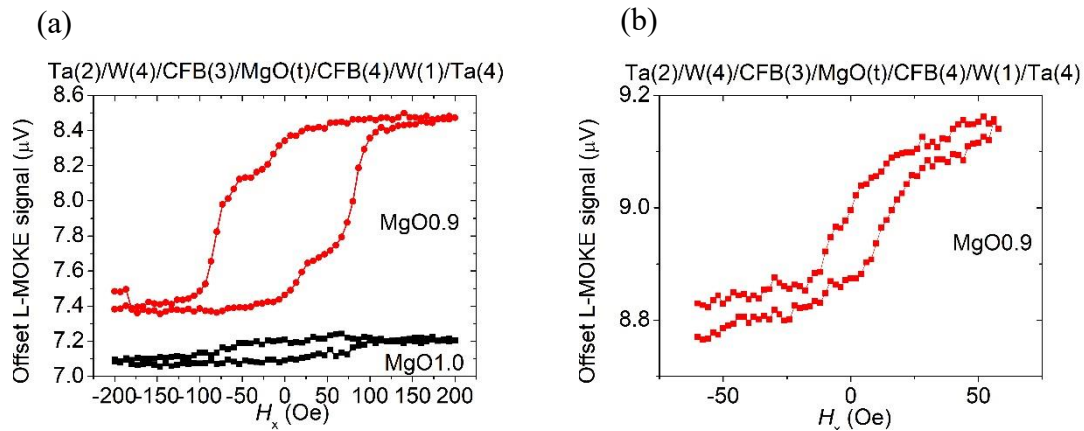


Figure 4.16 (a)(b) It shows double loops only for MgO thickness at 0.9nm, after annealing for 40 minutes.

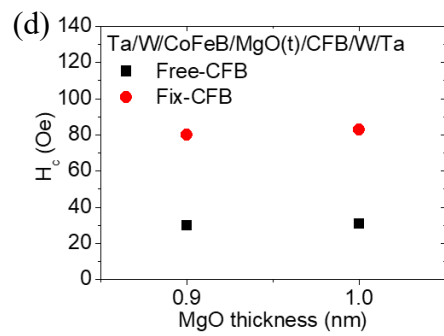
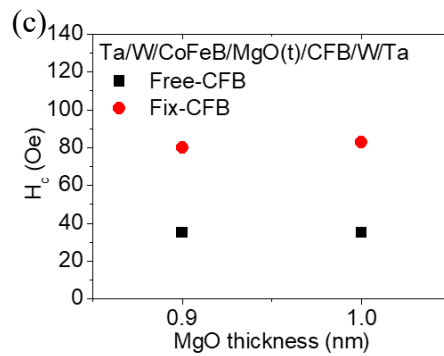
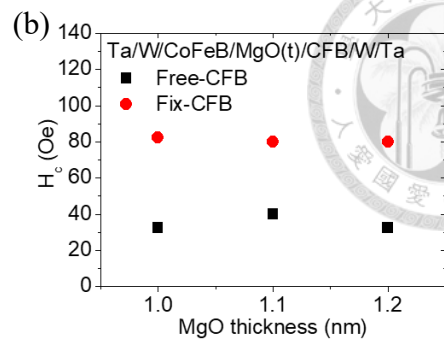
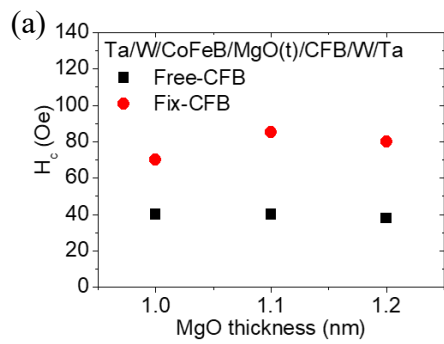


Figure 4.17 (a)(b)(c)(d) H_c shows similar results for different annealing time.

4.3.3 Short Conclusion

For half MTJ structures, we choose bottom half structure Ta(2)/W(4)/CFB(3)/MgO(1.5)/Ta(4), and top half structure MgO(1.5)/CFB(4)/W(0.5)/Ta(4). Bottom half structures show evident easy and hard axes behaviors under 8000Oe. As for top half structure, however, doesn't show evident easy and hard axes behaviors.

For full MTJ structures, Ta(2)/W(4)/CFB(3)/MgO(0.9)/CFB(4)/W(1)/Ta(4) shows double loops. For different annealing time, H_c doesn't change.

4.4 Failure Analysis for MTJ Devices

4.4.1 Case 1 of Stop-on-W

We try to fabricate MTJ thin films into devices. The fabrication processes are illustrated in Chapter 2.3.1. In the 1st step, we define the device and electrodes by lithography and etching. In the 2nd step, we define the pillar by lithography, etching and E-beam evaporator. In the 3rd step, we define the electrode by lithography and depositing Ta and W. In the following chapter, we will demonstrate these processes. The two cases in Chapter 4.4.1 and Chapter 4.4.2 uses PMA thin films, while the case in Chapter 4.4.3 adopts IMA thin films.

Firstly, we detect the P-MOKE signal of the four thin films. All of them are deposited in the same layer order, as shown in Figure 4.20. Sample 1 and 2 show only single loop,



while sample 3 and 4 have double loop in Figure 4.18.

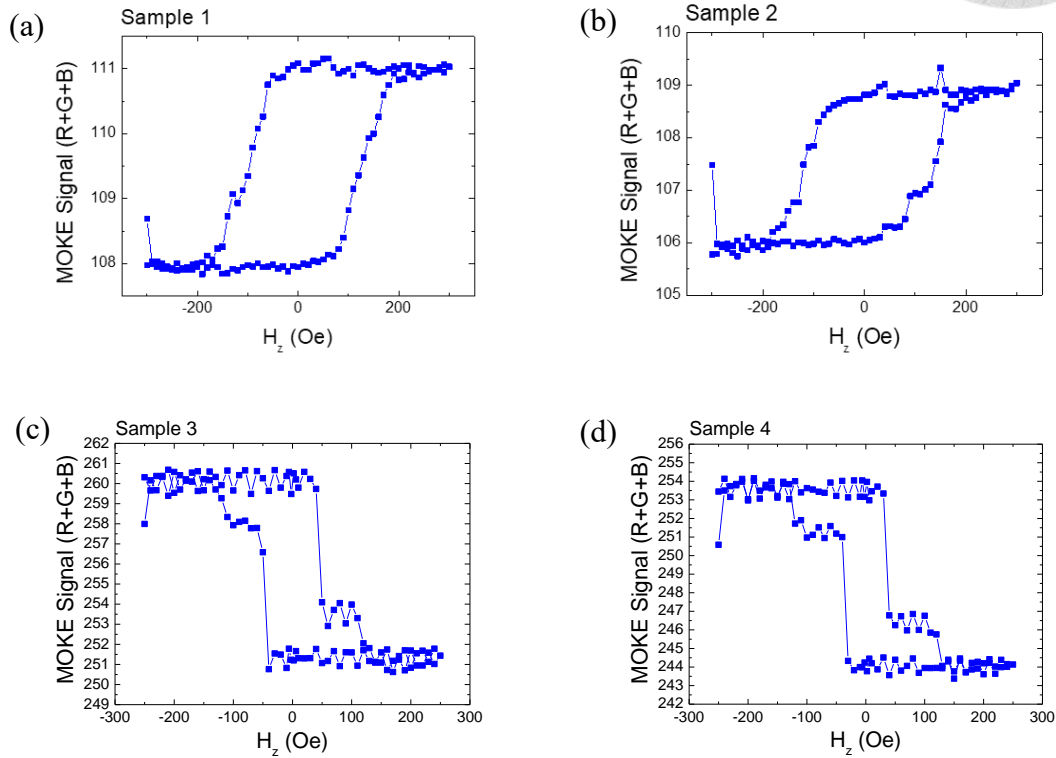
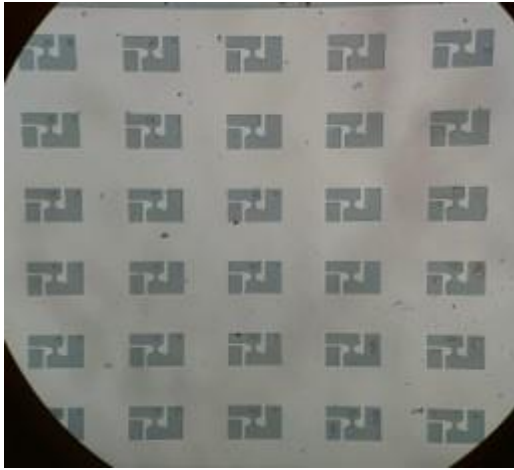


Figure 4.18 MOKE signal of four samples. (a)(b) PMA sample with one single hysteresis loop. (c)(d) PMA sample with double hysteresis loops.

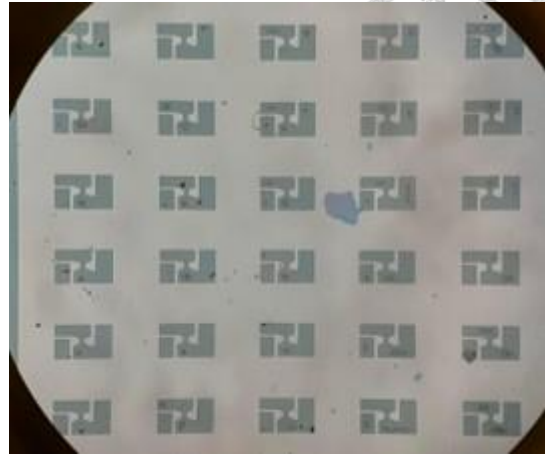
The OM image of the 1st lithography is shown in Figure 4.19. We define the devices and the electrode pads of “top” and “bottom” in the 1st step, which suggests how the electrode is connected to the top or bottom of the pillar. The 1st etching signal in Figure 4.20 shows the etching process. We etch to the Si substrate in the 1st step.

(a)

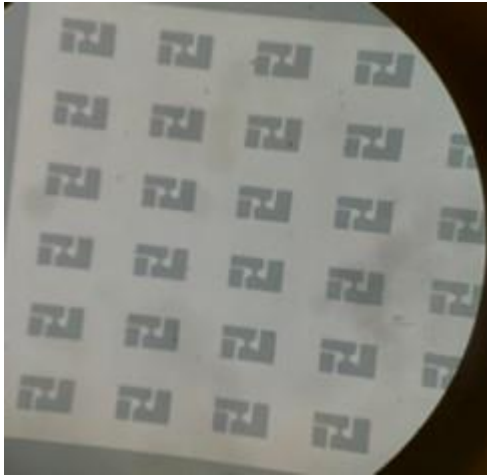
(b)



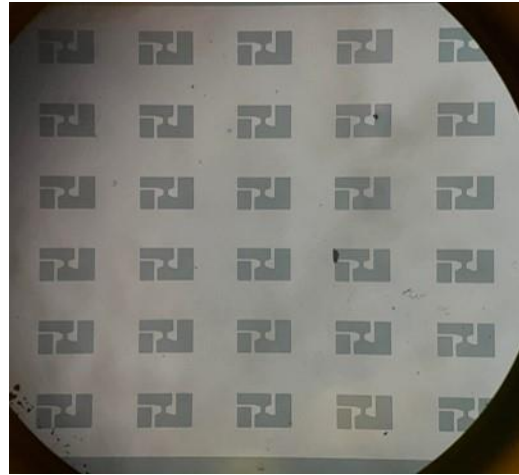
(c)



(d)



(e)



(f)

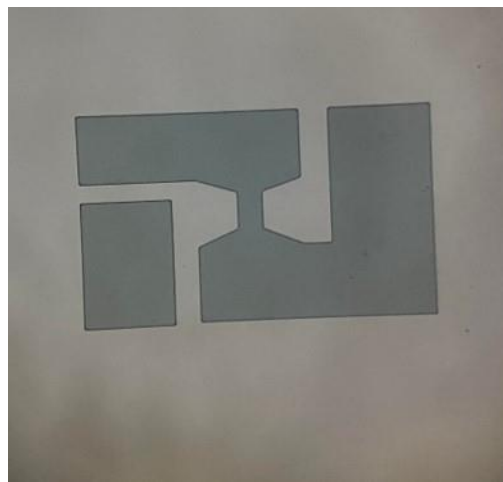
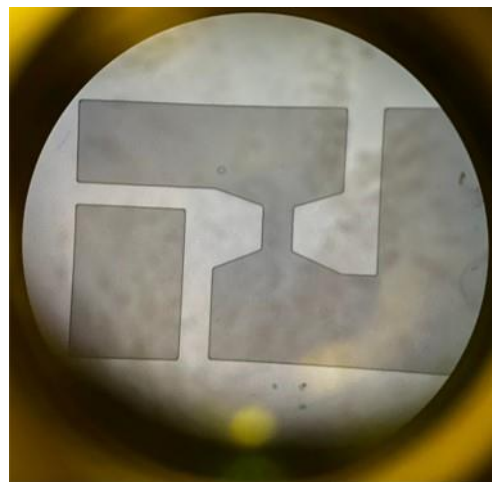


Figure 4.19 OM images of 1st lithography (a) Sample 1 (b) Sample 2 (c)(d) Sample 3

(e)(f) Sample 4

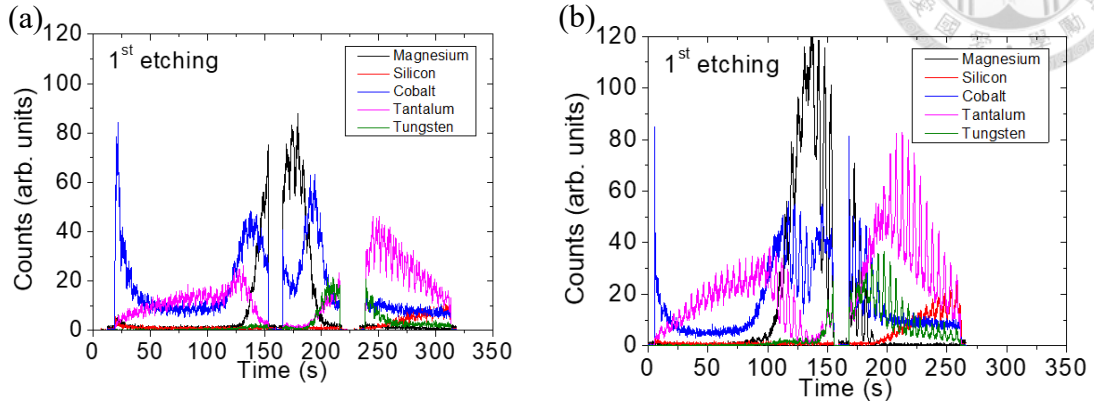
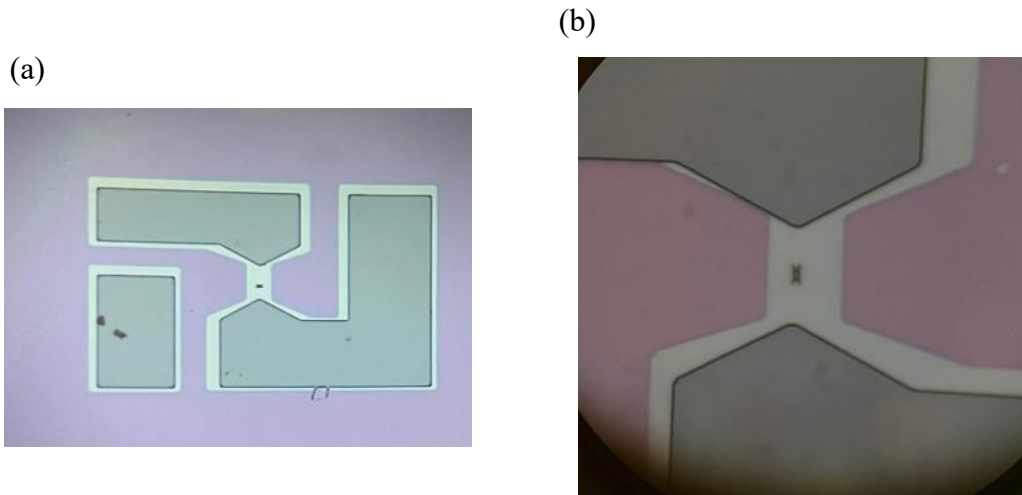


Figure 4.20 SIMS signal of 1st Etching (a) Sample 1 and 2 (b) Sample 3 and 4

The OM image of the 2nd lithography is shown in Figure 4.21. We define the pillar in the 2nd step. As shown in the 2nd etching signal, Figure 4.22, we stop on the W layer for the 2nd etching. We stop at about 7 seconds after W signal reaches 12 on intensity.



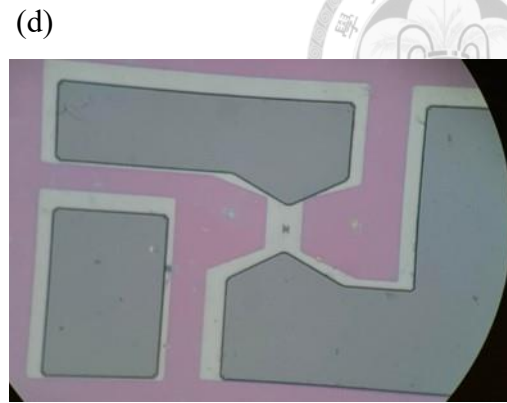
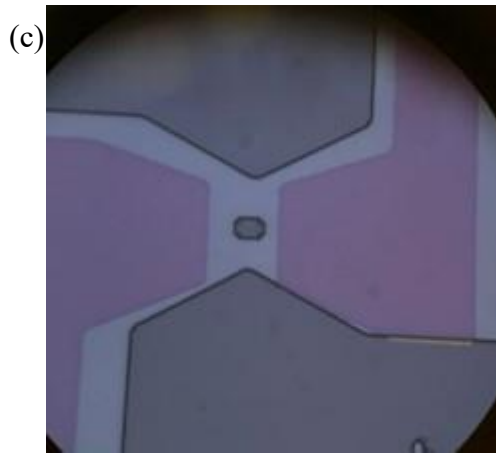


Figure 4.21 OM images of 2nd lithography (a) Sample 1 (b) Sample 2 (c) Sample 3 (d) Sample 4

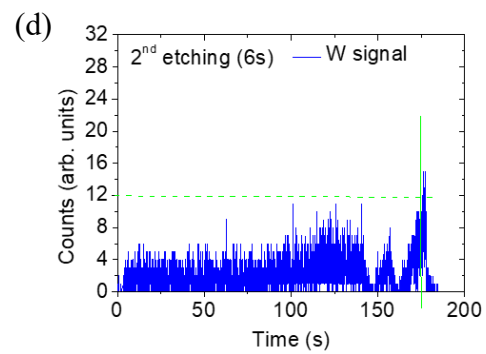
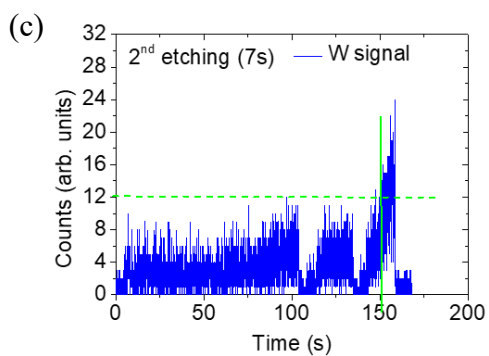
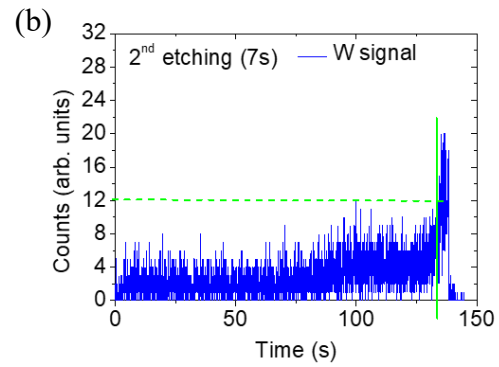
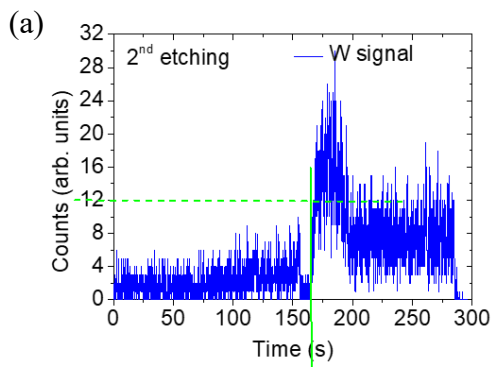


Figure 4.22 2nd etching (a)(b)(c)(d) stands for sample 1 to 4 respectively.

The OM image of after depositing electrode in the 3rd step is shown in Figure 4.23.

We deposit the Ta and W electrode in the 3rd step. Figure 4.23(a) shows that the electrodes

on well deposited in sample 3, while some electrodes are not in sample 4.



(a)



(b)



Figure 4.23 OM image of 3rd lithography (a) Sample 3 (b) Sample 4

After the three steps, we detect the electric signals. However, the signals don't show as expected. Sample 1 & 4 overflowed on signal. Little signal shows on sample 2 and 3.

For sample 2, in Figure 4.24 and Figure 4.25, only 1 device show TMR signal on both top-to-bottom and bottom-to-bottom detection.

For sample 3, 4 devices show TMR signal on top-to-bottom detection and 3 devices on bottom-to-bottom detection, as in Figure 4.26 and Figure 4.27. The highest TMR ratio of top-to-bottom is about 5.19%. We then count the TMR resistance and TMR ratio of top-to-bottom signal in Figure 4.28, and that of bottom-to-bottom signal in Figure 4.29.

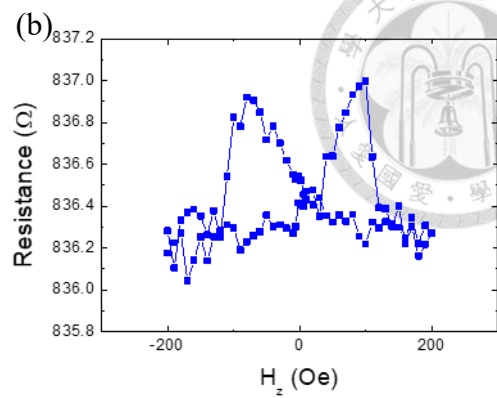
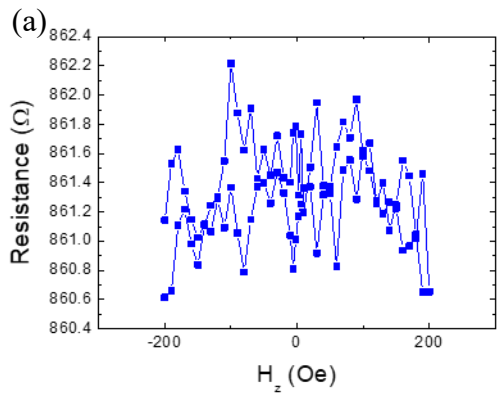


Figure 4.24 Top-to-bottom signal for sample 2 (a) $12 \times 10 \mu\text{m}^2$ (b) $12 \times 6 \mu\text{m}^2$

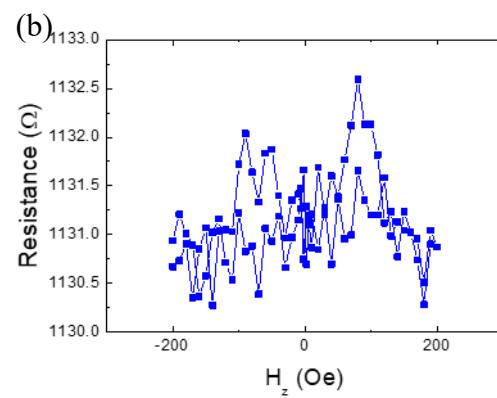
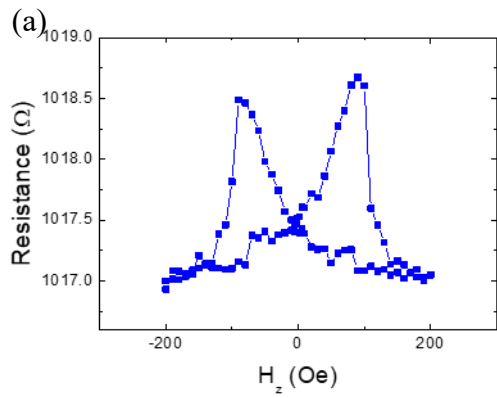


Figure 4.25 Bottom-to-bottom signal for sample 2 (a) $12 \times 10 \mu\text{m}^2$ (b) $12 \times 6 \mu\text{m}^2$

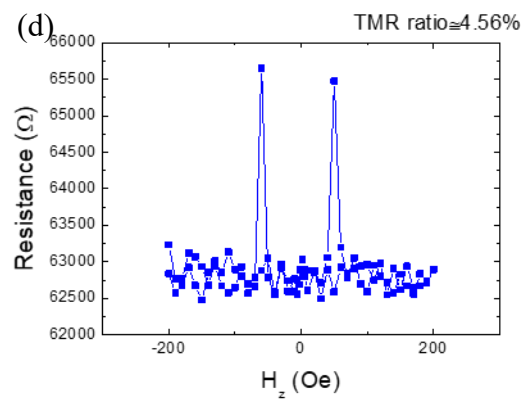
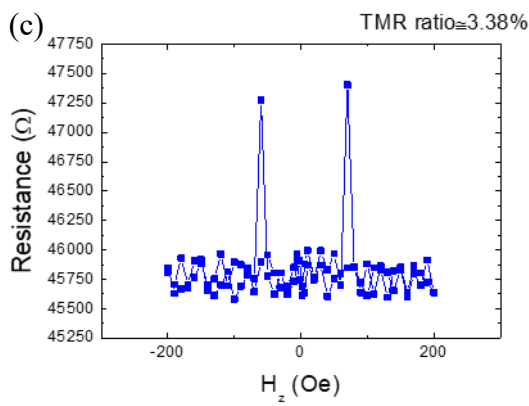
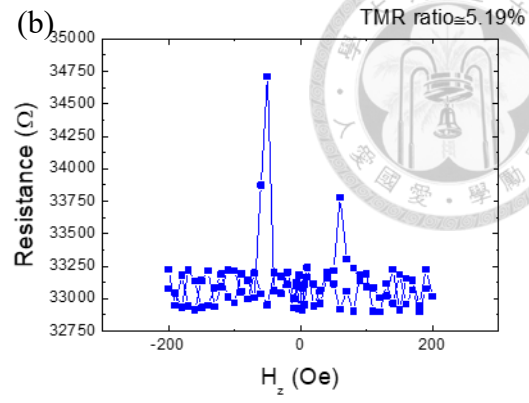
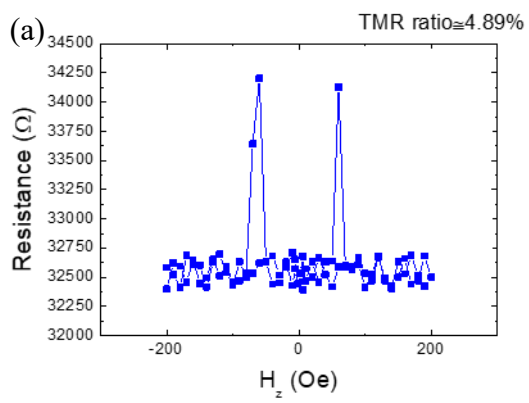


Figure 4.26 Top-to-bottom signal for sample 3 (a) $12 \times 10 \mu\text{m}^2$ (b) $12 \times 6 \mu\text{m}^2$ (c) $10 \times 8 \mu\text{m}^2$
(b) $8 \times 6 \mu\text{m}^2$

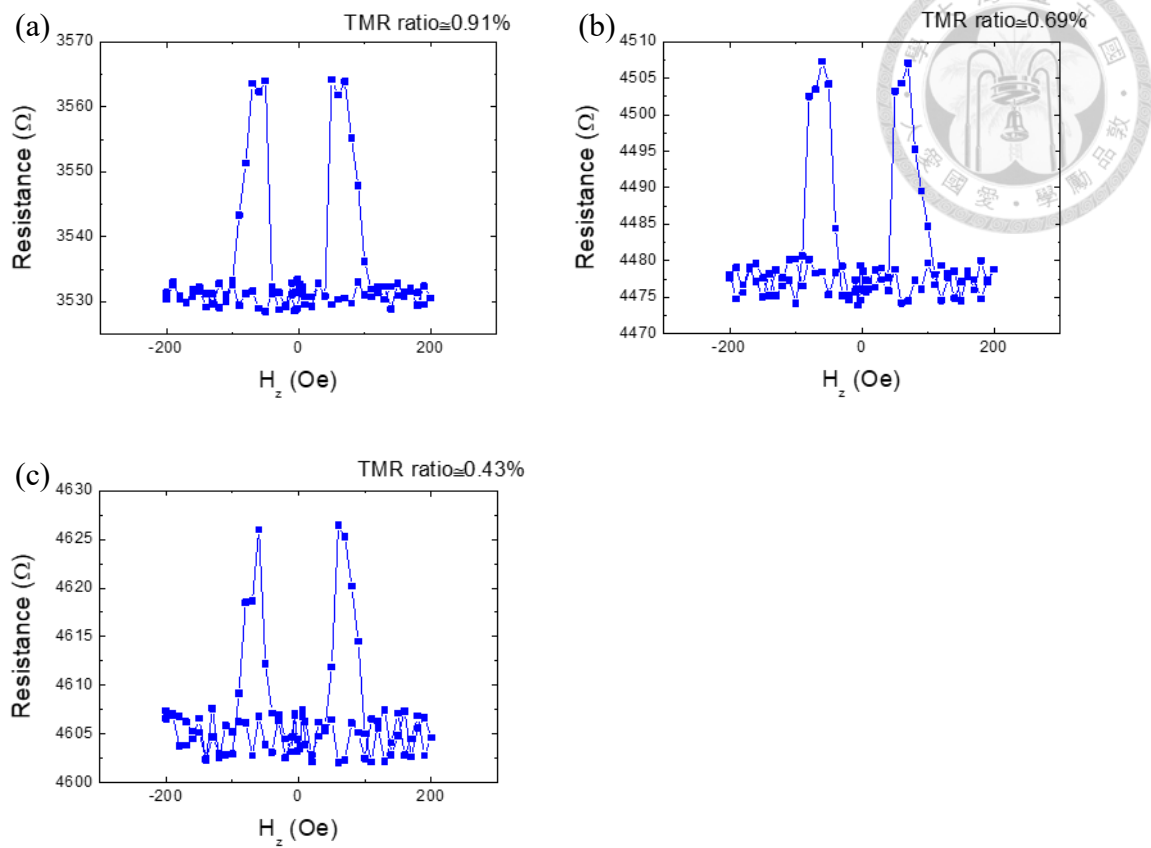


Figure 4.27 Bottom-to-bottom signal for sample 3 (a) $12 \times 10 \mu\text{m}^2$ (b) $10 \times 8 \mu\text{m}^2$ (c) $8 \times 6 \mu\text{m}^2$

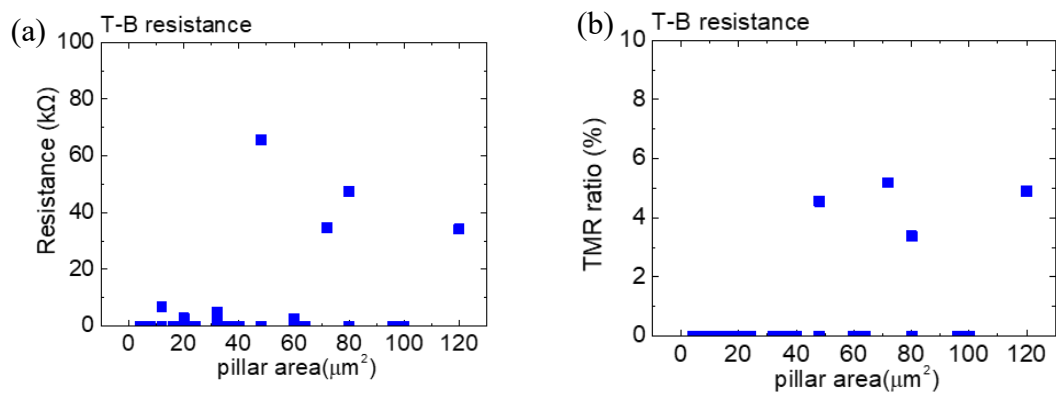


Figure 4.28 Top-to-bottom signal for sample 3 (a) Resistance relation to pillar area (b) TMR ratio

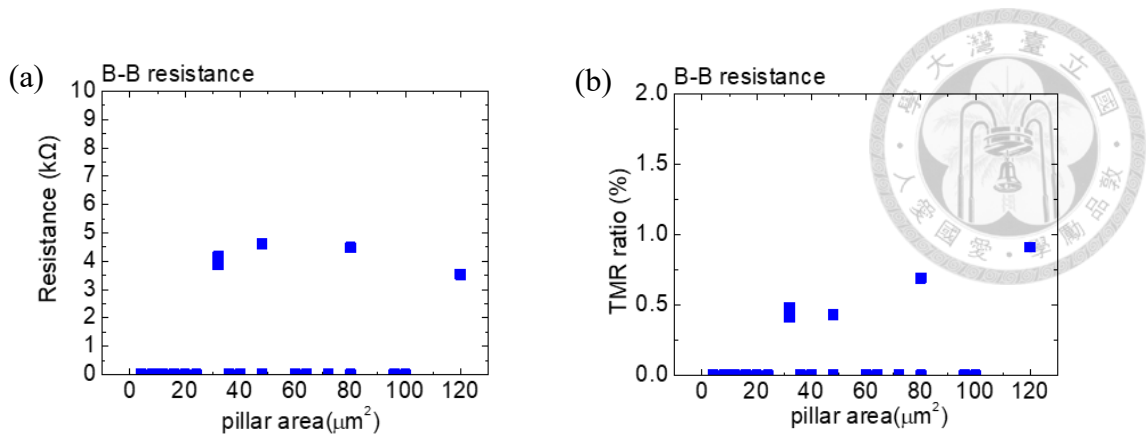


Figure 4.29 Bottom-to-bottom signal for sample 3 (a) Resistance relation to pillar area
(b) TMR ratio

4.4.2 Case 2 of Stop-on-W

After the case above, we perform similar fabrication process again. During last fabrication, some processes were not well performed; therefore, this time, we make sure that every step is performed correctly.

As shown in Figure 4.30 and Figure 4.31, again we perform 1st etching to the device, until Si shows larger signal than Ta. We then perform 2nd etching until W signal raises to 12, based on the etching time acquired in 1st etching. Since the whole fabrication process is similar on OM image, we demonstrate only the crucial etching processes here.

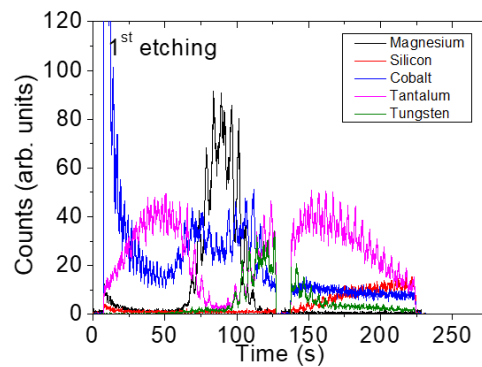


Figure 4.30 1st etching signal of the sample

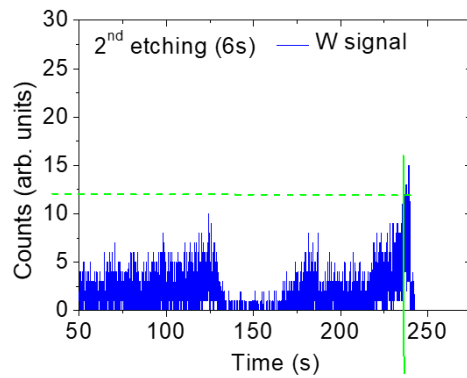
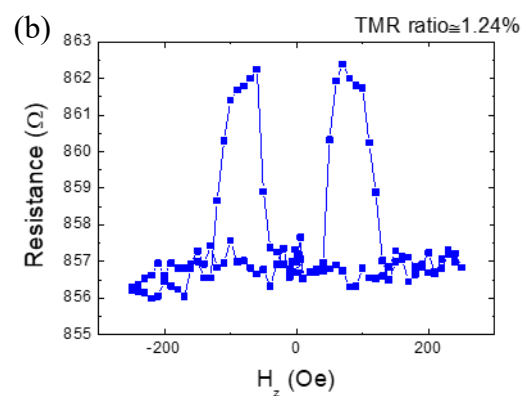
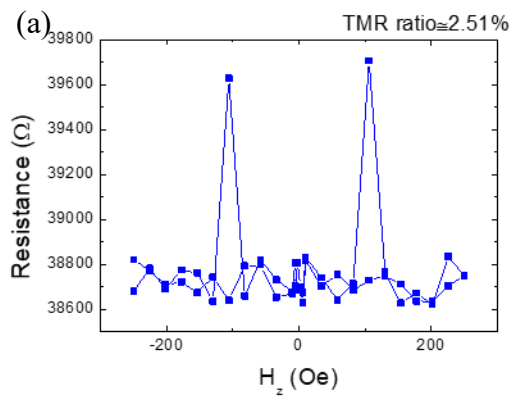


Figure 4.31 2nd etching signal of the sample

After the whole fabrication, we detect the TMR signal on both top-to-bottom and bottom-to-bottom, respectively in Figure 4.32 and Figure 4.33. For top-to-bottom signal, only four devices show TMR loop, with the highest switching ratio at 2.51% this time. As for bottom-to-bottom detection, three devices show TMR loop.



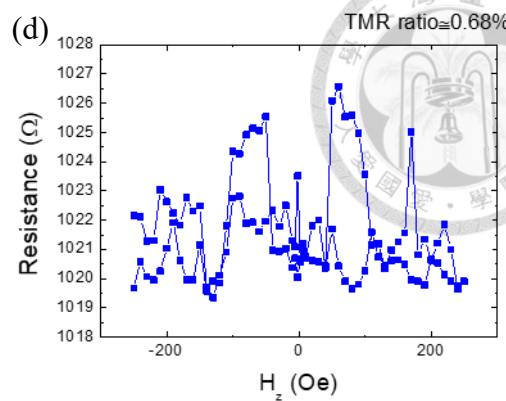
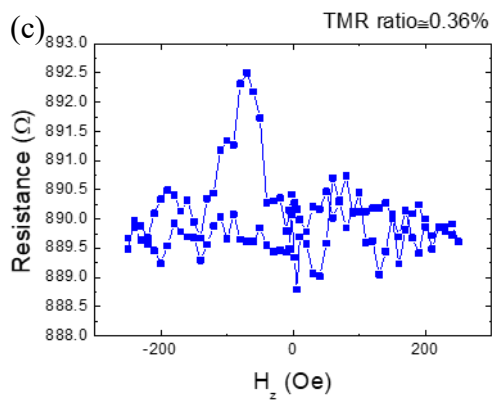


Figure 4.32 Top-to-bottom signal (a) $12 \times 10 \mu\text{m}^2$ (b) $10 \times 8 \mu\text{m}^2$ (c) $4 \times 8 \mu\text{m}^2$ (d) $2 \times 6 \mu\text{m}^2$

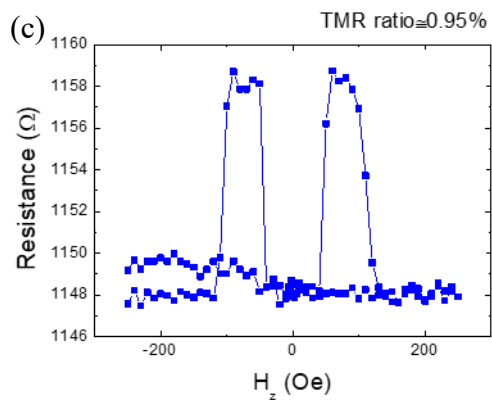
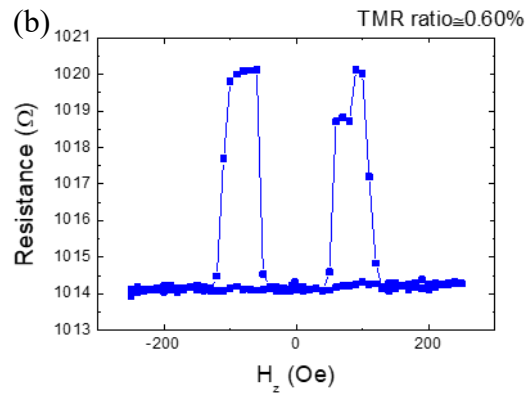
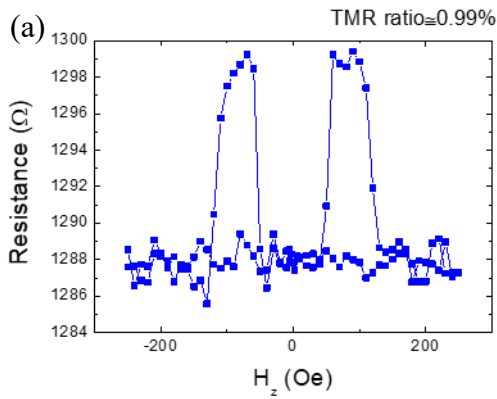


Figure 4.33 Bottom-to-bottom signal (a) $12 \times 10 \mu\text{m}^2$ (b) $10 \times 8 \mu\text{m}^2$ (c) $4 \times 8 \mu\text{m}^2$

4.4.3 Case 3 Stop-on-MgO

Since we failed on previous attempts, we decide to change the stop layer to MgO

this time. The 1st process in Figure 4.34 is similar to Chapter 4.4.1, case stop-on-W.

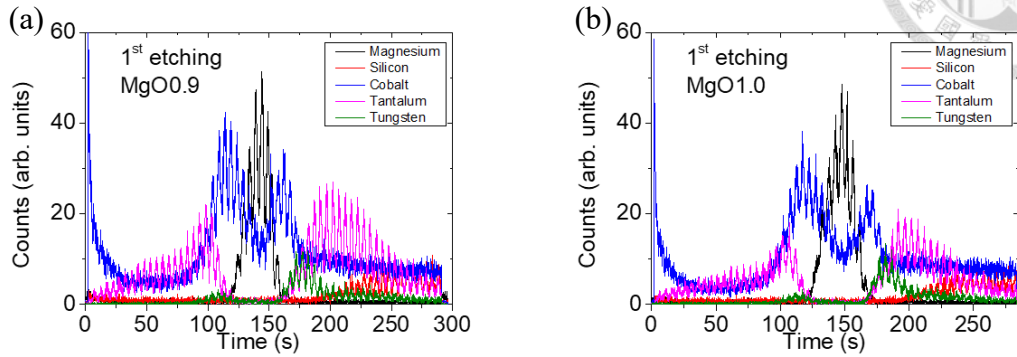
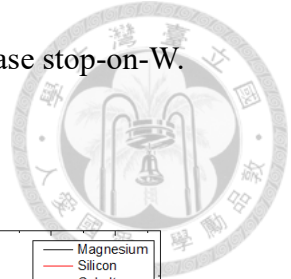
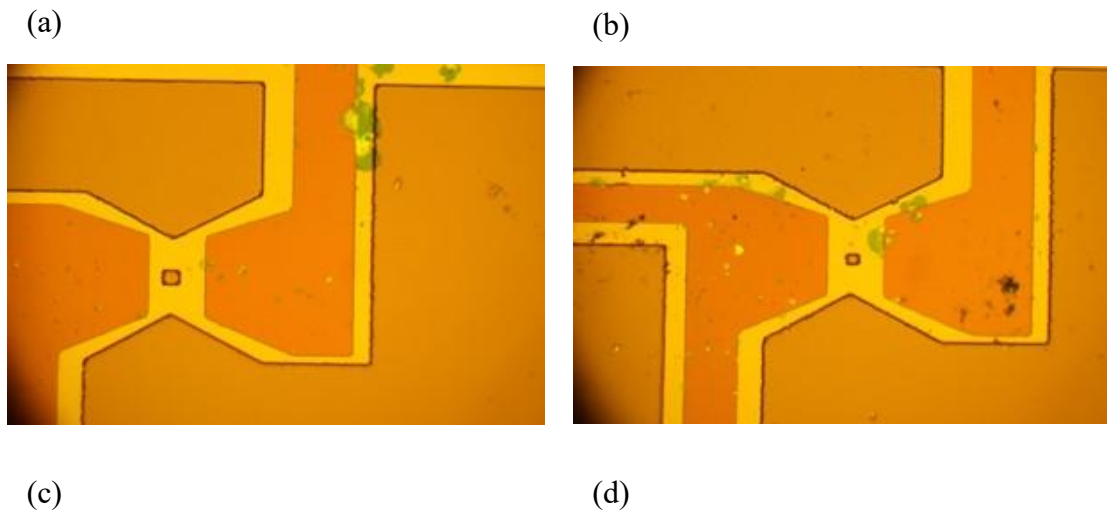


Figure 4.34 1st etching signal of case stop-on-MgO

In Figure 4.35, 2nd lithography, we make sure the pillar is clear shown under OM image. For the 2nd etching this time, Figure 4.36, we stop on MgO layer, when Mg signal reaches 3 on signal. In Figure 4.37, we can still clearly see the pillar after depositing SiO₂ with E-gun evaporation and lift-off.



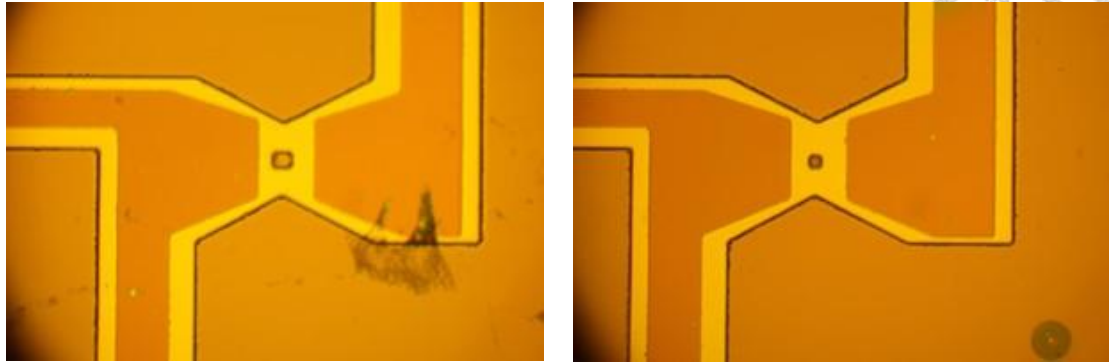


Figure 4.35 (a)(b)(c)(d) OM images of 2nd lithography

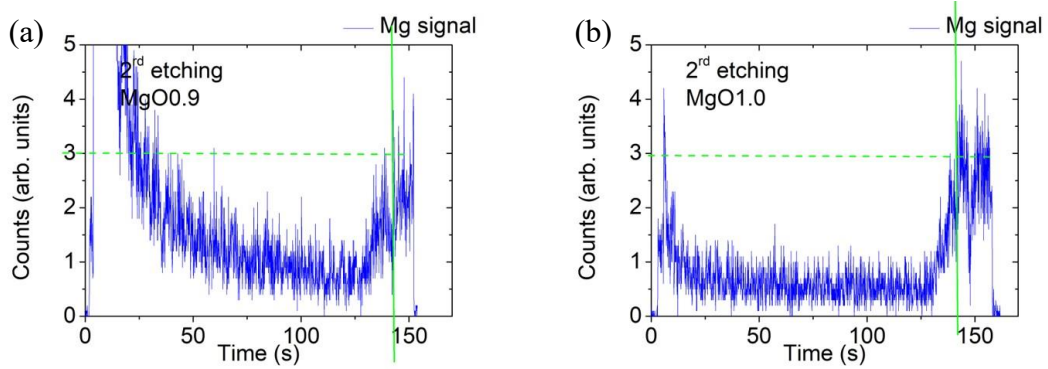
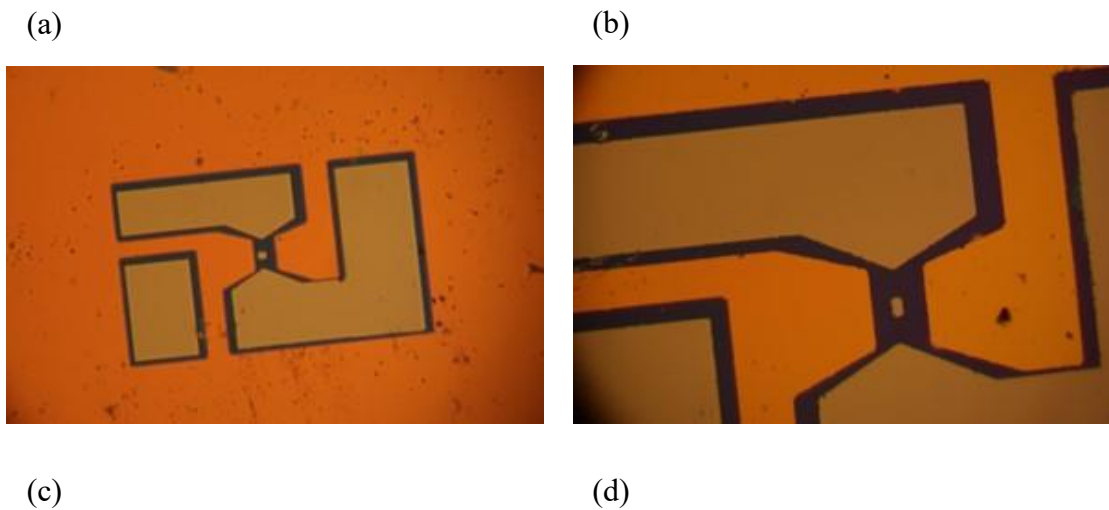


Figure 4.36 2nd etching signal of case stop-on-MgO



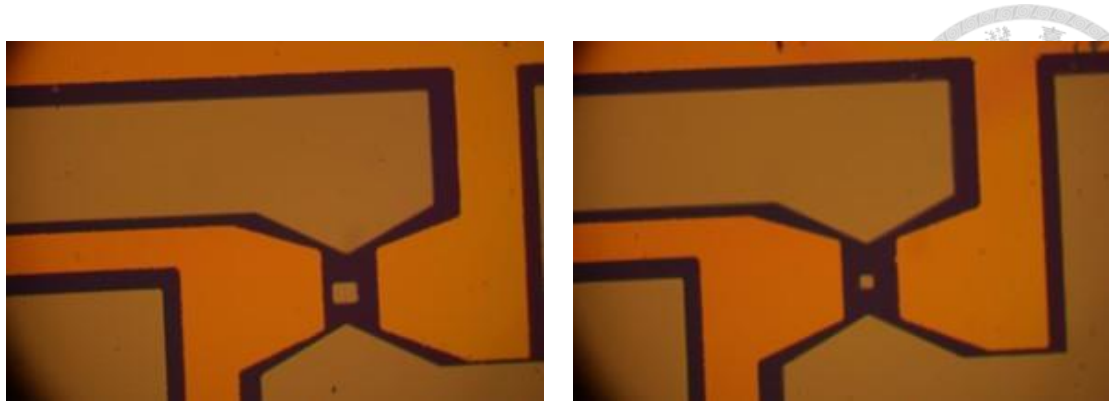


Figure 4.37 OM images of 2nd E-gun evaporation

For the 3rd lithography, Figure 4.38, we can see the pillar after lithography. We then deposit Ta and W atop.

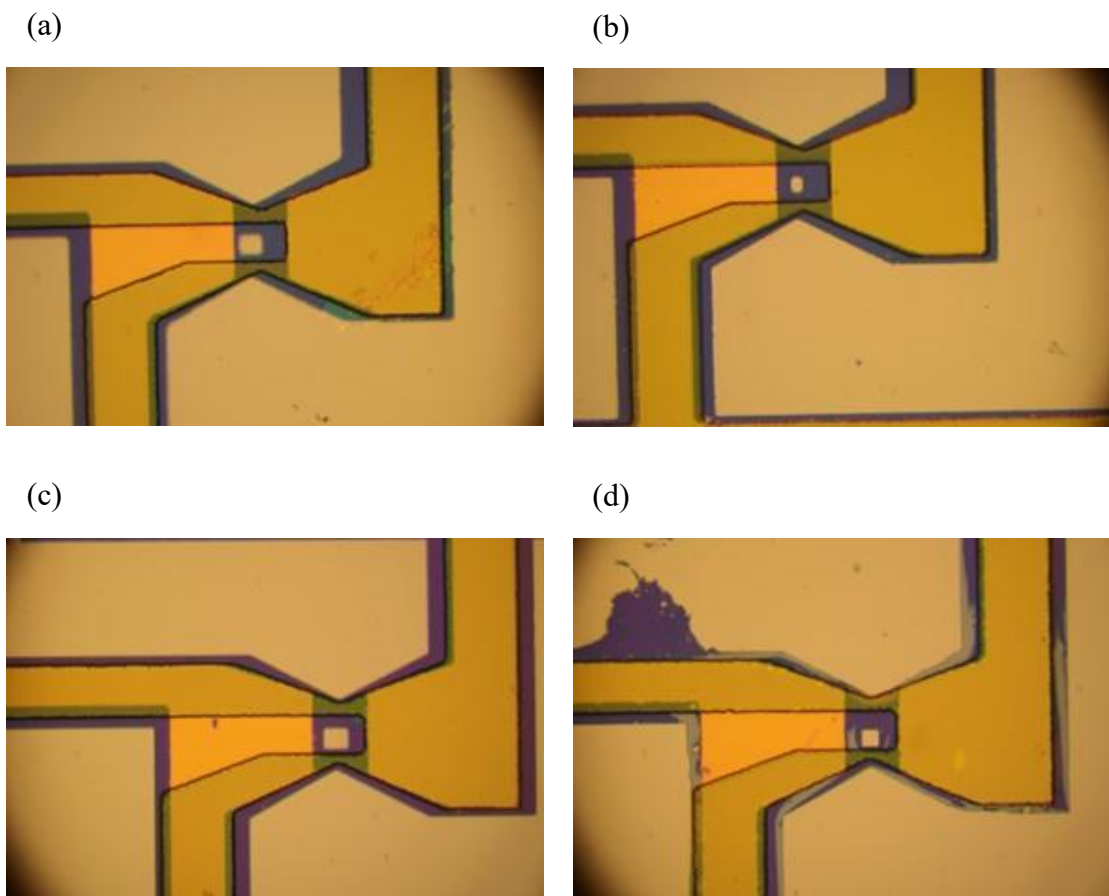


Figure 4.38 OM images of 3rd lithography

After fabrication, we again detect the signals. For Figure 4.39, only one device of sample MgO 1.0 shows TMR loop for top-to-bottom detection. Other devices fail for both top-to-bottom and bottom-to-bottom detection, Figure 4.40 and Figure 4.41 respectively. We then count the distribution of resistivity for top-to-bottom for the two samples.

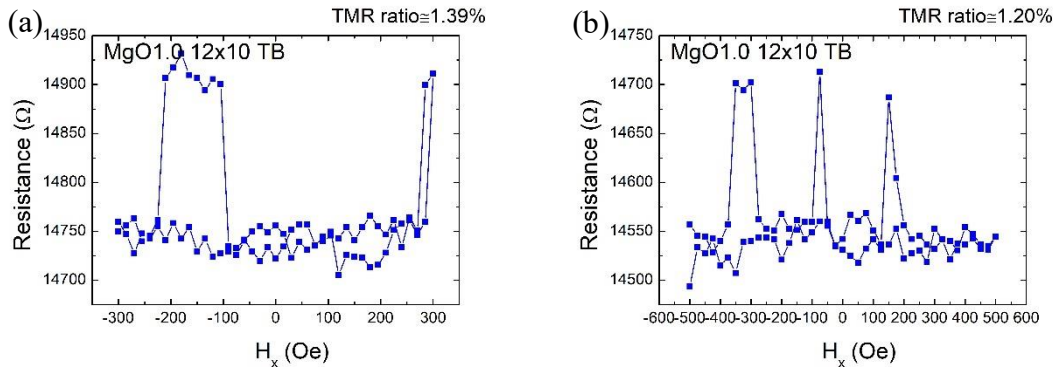


Figure 4.39 (a)(b) One device of sample MgO 1.0 shows TMR loop for top-to-bottom detection

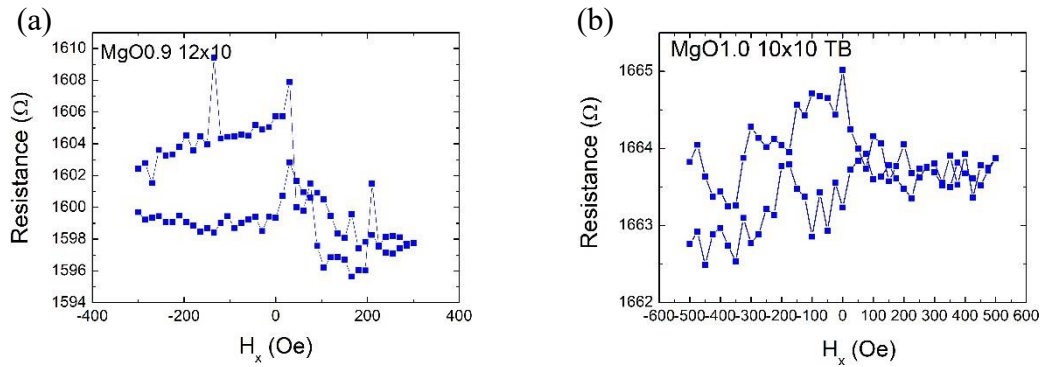


Figure 4.40 Fail devices of sample MgO 0.9 and MgO 1.0 for top-to-bottom signal (a) MgO0.9 12x10 μm^2 (b) MgO1.0 10x10 μm^2

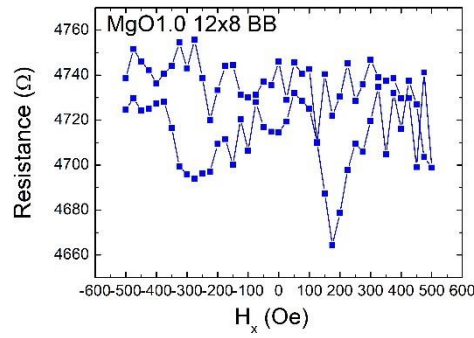


Figure 4.41 Fail devices of sample MgO 1.0 for bottom-to-bottom signal, $12 \times 8 \mu\text{m}^2$

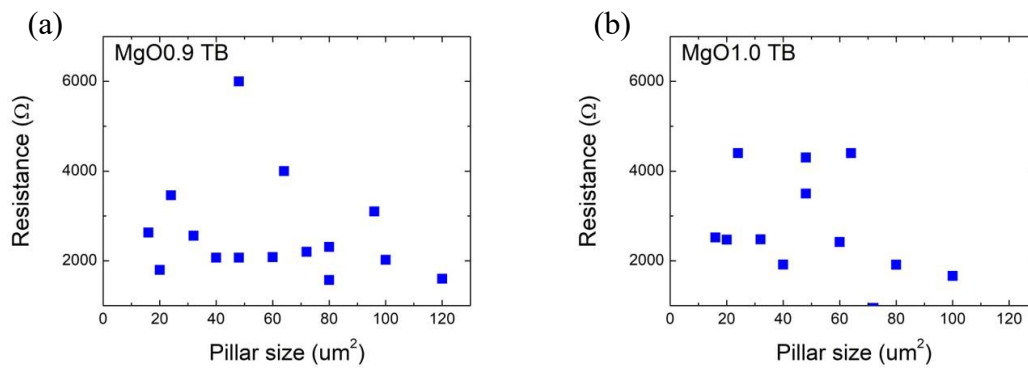


Figure 4.42 Resistance distribution of sample MgO 0.9 and MgO 1.0

4.4.4 Short Conclusion

We demonstrate a workflow of MTJ device fabrication, including three cases, two stop-on-W and one stop-on-MgO.

In the first stop-on-W case, we demonstrate our process of three lithography steps, with etching, E-gun evaporation or depositing electrodes afterward. After fabrication, some devices show TMR loop, on either top-to-bottom or bottom-to-bottom detection.

We perform stop-on-W case the second time. It shows similar results. Some devices show TMR loop, on the two detection.

For the third time, we change the stop layer to MgO. One device shows TMR loop

on top-to-bottom detection.



Chapter 5 Summary



Firstly in PMA MTJ thin films, we determine the best thickness with appropriate H_c . For half MTJ structure, we find Ta(2)/W(4)/CFB(1.6)/MgO(1.5)/Ta(4) and MgO(1.5)/CFB(2.0)/W(0.5)/Ta(4), to be the best structures, for bottom and top half structures, respectively. Later in full MTJ structure, we modulate CoFeB, MgO and W thickness and acquire double loop in the structure Ta(2)/W(4)/CFB(1.6)/MgO(1.2)/CFB(2.0)/W(0.7)/Ta(4).

Secondly in IMA MTJ thin films, we find Ta(2)/W(4)/CFB(3.0)/MgO(1.5)/Ta(4) and MgO(1.5)/CFB(t)/W(0.5)/Ta(4), where $t = 4.0, 4.5, 5.0, 5.5$, to be the best structures, for bottom and top half structures respectively. For full MTJ structure, double loop can be obtained in the structures Ta(2)/W(4)/CFB(3)/MgO(t)/CFB(4)/W(1)/Ta(4), $t = 1.2, 1.3, 1.4, 1.5$. For as-deposited thin films and thin films with different annealing time, we demonstrate that annealing can significantly increase coercivity, while double loops exist in different annealing time, 20, 30, 40 and 50 minutes. Also, we find out these thin films do not have evident regulation on different angle.

Thirdly in IMA MTJ thin films annealed by external field 8000Oe, bottom half structure Ta(2)/W(4)/CFB(3)/MgO(1.5)/Ta(4) shows evident easy and hard axes behavior, while top half structure MgO(1.5)/CFB(4)/W(0.5)/Ta(4) does not. Full MTJ structures, Ta(2)/W(4)/CFB(3)/MgO(0.9)/CFB(4)/W(1)/Ta(4), shows double loops. Also, annealing with external field does not increase coercivity.

Lastly in MTJ fabrication, we demonstrate a workflow to fabricate an MTJ device with two methods, stop-on-W and one stop-on-MgO. In the stop-on-W cases, we demonstrate the fabrication process and TMR detection. Some devices show TMR signals,

in both top-to-bottom and bottom-to-bottom detection. As for the stop-on-MgO case, one device shows TMR loop in top-to-bottom detection.



REFERENCE




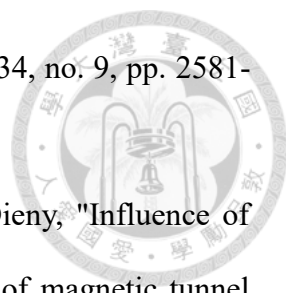
- [1] P. Sandgren and I. Snowball, "Application of Mineral Magnetic Techniques to Paleolimnology," in *Tracking Environmental Change Using Lake Sediments: Physical and Geochemical Methods*, W. M. Last and J. P. Smol Eds. Dordrecht: Springer Netherlands, 2001, pp. 217-237.
- [2] A. Renuka Balakrishna and R. D. James, "A tool to predict coercivity in magnetic materials," *Acta Materialia*, vol. 208, p. 116697, 2021/04/15/ 2021, doi: <https://doi.org/10.1016/j.actamat.2021.116697>.
- [3] M. Julliere, "Tunneling between ferromagnetic films," *Physics Letters A*, vol. 54, no. 3, pp. 225-226, 1975/09/08/ 1975, doi: [https://doi.org/10.1016/0375-9601\(75\)90174-7](https://doi.org/10.1016/0375-9601(75)90174-7).
- [4] S. Ikeda *et al.*, "Tunnel magnetoresistance of 604% at 300K by suppression of Ta diffusion in CoFeB / MgO / CoFeB pseudo-spin-valves annealed at high temperature," *Applied Physics Letters*, vol. 93, no. 8, 2008, doi: 10.1063/1.2976435.
- [5] P. Carcia, A. Meinhardt, and A. Suna, "Perpendicular magnetic anisotropy in Pd/Co thin film layered structures," *Applied Physics Letters*, vol. 47, no. 2, pp. 178-180, 1985.
- [6] S. Ikeda *et al.*, "A perpendicular-anisotropy CoFeB–MgO magnetic tunnel junction," *Nature Materials*, vol. 9, no. 9, pp. 721-724, 2010/09/01 2010, doi: 10.1038/nmat2804.
- [7] M. N. Baibich *et al.*, "Giant magnetoresistance of (001)Fe/(001)Cr magnetic superlattices," *Phys Rev Lett*, vol. 61, no. 21, pp. 2472-2475, Nov 21 1988, doi:


- 10.1103/PhysRevLett.61.2472.
- [8] N. F. Mott, "The resistance and thermoelectric properties of the transition metals," *Proceedings of the Royal Society of London. Series A - Mathematical and Physical Sciences*, vol. 156, no. 888, pp. 368-382, 1936, doi: doi:10.1098/rspa.1936.0154.
- [9] N. F. Mott, "Electrons in transition metals," *Advances in Physics*, vol. 13, no. 51, pp. 325-422, 1964.
- [10] S. S. P. Parkin, R. Bhadra, and K. P. Roche, "Oscillatory magnetic exchange coupling through thin copper layers," *Physical Review Letters*, vol. 66, no. 16, pp. 2152-2155, 04/22/ 1991, doi: 10.1103/PhysRevLett.66.2152.
- [11] R. Nakatani, T. Dei, and Y. Sugita, "Oscillation of magnetoresistance in [Ni-Fe/Cu]20/Cu/Fe multilayers with thickness of Cu spacer neighboring Fe buffer layer," *Journal of Applied Physics*, vol. 73, no. 10, pp. 6375-6377, 1993, doi: 10.1063/1.352655.
- [12] S. Bouat, B. Rodmacq, and P. Auric, "Transmission X-Ray Diffraction and Mössbauer Spectroscopy Study of Annealed Magnetoresistive Ag/Ni₈Fe₉ Multilayers," *MRS Online Proceedings Library*, vol. 475, no. 1, pp. 291-296, 1997/12/01 1997, doi: 10.1557/PROC-475-291.
- [13] S. S. P. Parkin, R. F. C. Farrow, R. F. Marks, A. Cebollada, G. R. Harp, and R. J. Savoy, "Oscillations of interlayer exchange coupling and giant magnetoresistance in (111) oriented permalloy/Au multilayers," *Physical Review Letters*, vol. 72, no. 23, pp. 3718-3721, 06/06/ 1994, doi: 10.1103/PhysRevLett.72.3718.
- [14] Y. Yao *et al.*, "Tunneling magnetoresistance materials and devices for neuromorphic computing," *Materials Futures*, 2023.
- [15] Y. T. Evgeny, N. M. Oleg, and R. L. Patrick, "Spin-dependent tunnelling in magnetic tunnel junctions," *Journal of Physics: Condensed Matter*, vol. 15, no. 4,

- p. R109, 2003/01/20 2003, doi: 10.1088/0953-8984/15/4/201.
- [16] W. Butler, X.-G. Zhang, T. Schulthess, and J. MacLaren, "Spin-dependent tunneling conductance of Fe|MgO|Fe sandwiches," *Physical Review B*, vol. 63, no. 5, p. 054416, 2001.
- [17] J. Mathon and A. Umerski, "Theory of tunneling magnetoresistance of an epitaxial Fe/MgO/Fe(001) junction," *Physical Review B*, vol. 63, no. 22, p. 220403, 05/10/2001, doi: 10.1103/PhysRevB.63.220403.
- [18] S. Yuasa, K. Hono, G. Hu, and D. C. Worledge, "Materials for spin-transfer-torque magnetoresistive random-access memory," *MRS Bulletin*, vol. 43, no. 5, pp. 352-357, 2018/05/01 2018, doi: 10.1557/mrs.2018.93.
- [19] Y. S. Choi, K. Tsunekawa, Y. Nagamine, and D. Djayaprawira, "Transmission electron microscopy study on the polycrystalline CoFeB / MgO / CoFeB based magnetic tunnel junction showing a high tunneling magnetoresistance, predicted in single crystal magnetic tunnel junction," *Journal of Applied Physics*, vol. 101, no. 1, 2007, doi: 10.1063/1.2407270.
- [20] S. Yuasa, T. Nagahama, A. Fukushima, Y. Suzuki, and K. Ando, "Giant room-temperature magnetoresistance in single-crystal Fe/MgO/Fe magnetic tunnel junctions," *Nature Materials*, vol. 3, no. 12, pp. 868-871, 2004/12/01 2004, doi: 10.1038/nmat1257.
- [21] "University and Educational Intelligence," *Nature*, vol. 21, no. 537, pp. 361-361, 1880/02/01 1880, doi: 10.1038/021361b0.
- [22] E. H. Hall, "XVIII. On the "Rotational Coefficient" in nickel and cobalt," *The London, Edinburgh, and Dublin Philosophical Magazine and Journal of Science*, vol. 12, no. 74, pp. 157-172, 1881.
- [23] H. Weng, X. Dai, and Z. Fang, "From anomalous hall effect to the quantum

- anomalous hall effect," *arXiv preprint arXiv:1509.05507*, 2015.
- [24] M. I. Dyakonov and V. I. Perel, "Current-induced spin orientation of electrons in semiconductors," *Physics Letters A*, vol. 35, no. 6, pp. 459-460, 1971/07/12/ 1971, doi: [https://doi.org/10.1016/0375-9601\(71\)90196-4](https://doi.org/10.1016/0375-9601(71)90196-4).
- [25] Y. Kato, R. Myers, A. Gossard, and D. Awschalom, "Coherent spin manipulation without magnetic fields in strained semiconductors," *Nature*, vol. 427, no. 6969, pp. 50-53, 2004.
- [26] J. Wunderlich, B. Kaestner, J. Sinova, and T. Jungwirth, "Experimental Observation of the Spin-Hall Effect in a Two-Dimensional Spin-Orbit Coupled Semiconductor System," *Physical Review Letters*, vol. 94, no. 4, p. 047204, 02/04/ 2005, doi: 10.1103/PhysRevLett.94.047204.
- [27] L. H. Thomas, "The Motion of the Spinning Electron," *Nature*, vol. 117, no. 2945, pp. 514-514, 1926/04/01 1926, doi: 10.1038/117514a0.
- [28] W. Tang, H. Liu, Z. Li, A. Pan, and Y.-J. Zeng, "Spin-Orbit Torque in Van der Waals-Layered Materials and Heterostructures," *Advanced Science*, vol. 8, no. 18, p. 2100847, 2021, doi: <https://doi.org/10.1002/advs.202100847>.
- [29] L. Berger, "Emission of spin waves by a magnetic multilayer traversed by a current," *Physical Review B*, vol. 54, no. 13, pp. 9353-9358, 10/01/ 1996, doi: 10.1103/PhysRevB.54.9353.
- [30] J. C. Slonczewski, "Current-driven excitation of magnetic multilayers," *Journal of Magnetism and Magnetic Materials*, vol. 159, no. 1-2, pp. L1-L7, 1996.
- [31] Y. Huai, F. Albert, P. Nguyen, M. Pakala, and T. Valet, "Observation of spin-transfer switching in deep submicron-sized and low-resistance magnetic tunnel junctions," *Applied Physics Letters*, vol. 84, no. 16, pp. 3118-3120, 2004, doi: 10.1063/1.1707228.

- 
- [32] R. De Rose, T. Zanotti, F. M. Puglisi, F. Crupi, P. Pavan, and M. Lanuzza, "STT-MTJ Based Smart Implication for Energy-Efficient Logic-in-Memory Computing," *Solid-State Electronics*, vol. 184, p. 108065, 2021/10/01/ 2021, doi: <https://doi.org/10.1016/j.sse.2021.108065>.
- [33] J.-H. Park, C. Park, T. Jeong, M. T. Moneck, N. T. Nufer, and J.-G. Zhu, "Co / Pt multilayer based magnetic tunnel junctions using perpendicular magnetic anisotropy," *Journal of Applied Physics*, vol. 103, no. 7, 2008, doi: 10.1063/1.2838754.
- [34] L. Liu, O. J. Lee, T. J. Gudmundsen, D. C. Ralph, and R. A. Buhrman, "Current-Induced Switching of Perpendicularly Magnetized Magnetic Layers Using Spin Torque from the Spin Hall Effect," *Physical Review Letters*, vol. 109, no. 9, p. 096602, 08/29/ 2012, doi: 10.1103/PhysRevLett.109.096602.
- [35] L. Liu, C. F. Pai, Y. Li, H. W. Tseng, D. C. Ralph, and R. A. Buhrman, "Spin-Torque Switching with the Giant Spin Hall Effect of Tantalum," *Science*, vol. 336, no. 6081, pp. 555-558, 2012, doi: 10.1126/science.1218197.
- [36] C.-F. Pai, L. Liu, Y. Li, H. W. Tseng, D. C. Ralph, and R. A. Buhrman, "Spin transfer torque devices utilizing the giant spin Hall effect of tungsten," *Applied Physics Letters*, vol. 101, no. 12, p. 122404, 2012, doi: 10.1063/1.4753947.
- [37] D. Zhu and W. Zhao, "Threshold Current Density for Perpendicular Magnetization Switching Through Spin-Orbit Torque," *Physical Review Applied*, vol. 13, no. 4, p. 044078, 04/30/ 2020, doi: 10.1103/PhysRevApplied.13.044078.
- [38] S. Yuasa *et al.*, "Magnetic tunnel junctions with single-crystal electrodes: A crystal anisotropy of tunnel magneto-resistance," *Europhysics Letters*, vol. 52, no. 3, p. 344, 2000/11/01 2000, doi: 10.1209/epl/i2000-00445-5.
- [39] J. G. Simmons, "Electric Tunnel Effect between Dissimilar Electrodes Separated

- 
- by a Thin Insulating Film," *Journal of Applied Physics*, vol. 34, no. 9, pp. 2581-2590, 1963, doi: 10.1063/1.1729774.
- [40] L. Cuchet, B. Rodmacq, S. Auffret, R. C. Sousa, and B. Dieny, "Influence of magnetic electrodes thicknesses on the transport properties of magnetic tunnel junctions with perpendicular anisotropy," *Applied Physics Letters*, vol. 105, no. 5, 2014, doi: 10.1063/1.4892450.
- [41] W. X. Wang, Y. Yang, H. Naganuma, Y. Ando, R. C. Yu, and X. F. Han, "The perpendicular anisotropy of Co₄₀Fe₄₀B₂₀ sandwiched between Ta and MgO layers and its application in CoFeB/MgO/CoFeB tunnel junction," *Applied Physics Letters*, vol. 99, no. 1, 2011, doi: 10.1063/1.3605564.
- [42] M. Zhu *et al.*, "A CoFeB/MgO/CoFeB perpendicular magnetic tunnel junction coupled to an in-plane exchange-biased magnetic layer," *Applied Physics Letters*, vol. 106, no. 21, 2015, doi: 10.1063/1.4921967.
- [43] M. Zhu, H. Chong, Q. B. Vu, R. Brooks, H. Stamper, and S. Bennett, "Study of CoFeB thickness and composition dependence in a modified CoFeB/MgO/CoFeB perpendicular magnetic tunnel junction," *Journal of Applied Physics*, vol. 119, no. 7, 2016, doi: 10.1063/1.4942166.
- [44] L. Zhao *et al.*, "Enhancement of Magnetic and Electric Transport Performance of Perpendicular Spin-Orbit Torque Magnetic Tunnel Junction by Stop-on-MgO Etching Process," *IEEE Electron Device Letters*, vol. 44, no. 3, pp. 408-411, 2023, doi: 10.1109/LED.2023.3236835.
- [45] N. Sato *et al.*, "CMOS Compatible Process Integration of SOT-MRAM with Heavy-Metal Bi-Layer Bottom Electrode and 10ns Field-Free SOT Switching with STT Assist," in *2020 IEEE Symposium on VLSI Technology*, 16-19 June 2020 2020, pp. 1-2, doi: 10.1109/VLSITechnology18217.2020.9265028.

- 
- [46] P. N. Hishimone, H. Nagai, and M. Sato, "Methods of fabricating thin films for energy materials and devices," in *Lithium-ion Batteries-Thin Film for Energy Materials and Devices*: IntechOpen, 2020.
- [47] Z. Wang, Y. Wu, D. Qi, W. Yu, and H. Zheng, "Progress in the design, nanofabrication, and performance of metalenses," *Journal of Optics*, vol. 24, no. 3, p. 033001, 2022/02/11 2022, doi: 10.1088/2040-8986/ac44d8.
- [48] N. Savvides, "Correction masks for large-area ion beam etching and figuring of optics," *Journal of Applied Physics*, vol. 99, no. 9, 2006, doi: 10.1063/1.2197035.
- [49] S. Ahmadi *et al.*, "The Role of Physical Techniques on the Preparation of Photoanodes for Dye Sensitized Solar Cells," *International Journal of Photoenergy*, vol. 2014, no. 1, p. 198734, 2014, doi: <https://doi.org/10.1155/2014/198734>.
- [50] S. Yamamoto and I. Matsuda, "Measurement of the Resonant Magneto-Optical Kerr Effect Using a Free Electron Laser," *Applied Sciences*, vol. 7, no. 7, p. 662, 2017. [Online]. Available: <https://www.mdpi.com/2076-3417/7/7/662>.
- [51] S. Åberg, "Development of MOKE spectrometer," Independent thesis Advanced level (professional degree) Student thesis, UPTEC Q, 23011, 2023. [Online]. Available: <http://urn.kb.se/resolve?urn=urn:nbn:se:uu:diva-515222>
- [52] "IMP EPD – End Point Detector." <https://www.hidenanalytical.com/wp-content/uploads/2022/01/IMP-EPD-new-format.pdf> (accessed.